https://doi.org/10.1016/j.engstruct.2023.117231

Test, modelling and design of a demountable stainless steel bar connection system for precast concrete pavements

Jiachen GUO[1], Tak-Ming CHAN[1,*], Yuhong WANG[1]

[1] Department of Civil and Environmental Engineering, The Hong Kong Polytechnic University, Hong Kong, China

* Corresponding author: tak-ming.chan@polyu.edu.hk

Abstract

To promote the reuse of precast concrete pavement units, an innovative demountable stainless steel bar connection system is proposed in this paper. Monotonic load tests were conducted to investigate the effects of the width of the stainless steel bar connection, the width and the end distance of the stainless steel plate on the mechanical behaviour of the proposed connection system. As localised concrete crushing was observed after tests, the stainless steel bar connection system was updated with an expanded contact area between concrete and steel. Test results revealed that specimens with the updated connection system exhibited high initial stiffness with low concrete compressive stress concentration. Finite element analysis (FEA) was then carried out to further investigate the parameters that affected the structural performance of the updated connection system. According to the deformations of the stainless steel bar connection and high-strength bolts, an analytical approach was developed to predict the design load of the proposed connection system. Design recommendations were finally summarised based on the obtained test and parametric analysis results to guide the demountable connection design.

Keywords

Demountable stainless steel bar connection system, compressive stress concentration, finite element analysis, analytical approach, design recommendations.

1. Introduction

Municipal road system is one of the most important components of urban infrastructure. With a rapid increase of traffic volume over the past 20 decades, pavement systems made of less durable materials like asphalt and early-strength concrete may suffer various damages within 5 to 10 years [1-3]. The construction of new pavement systems is also indispensable to promote the development of modern society. Therefore, there are two main tasks for transportation agencies, including: maintenance of existing pavements and construction of new ones [3, 4]. In contrast to asphalt pavements, despite higher durability and longer service life, cast in-situ concrete pavements generally call for longer traffic closure time to allow concrete to reach sufficient strength. As reported by Cookson [5], economic impacts of more than 160 billion Euros will be created by traffic congestion by 2025 in Europe. As a result, to minimise the duration of traffic closure, precast concrete pavement (PCP) technology, which fabricates concrete pavement units offsite with high quality and durability, is recommended in pavement construction and maintenance [2, 3]. According to the traffic data collected by Missouri Department of Transport (DOT), costs induced by traffic closure have been reduced by 25 percent with the application of PCP technology [6].

In jointed plain concrete pavements (JPCP), three types of joints are designed in pavement construction including contraction joints, expansion joints and construction joints. Among these joints, the design of contraction joints is the most important as concrete is an anisotropic material weak in tension. A well-designed contraction joint can effectively mitigate the initiation and propagation of horizontal tensile cracks caused by concrete shrinkage [3, 7]. To improve continuity at pavement joints, epoxy-coated steel dowel bars, referring to effective load transfer devices, are always installed along contraction joints to transfer loads between pavement slabs [2, 3, 8-14]. However, in spite of widespread applications of dowel bars for

nearly 100 years [15], there are still typical issues that need to be addressed.

- Localised concrete crushing: under vertical load, severe compressive stress concentration around dowel bars may lead to localised concrete crushing as shown in Fig.1(a) [9, 13, 16-21].
- Horizontal tensile cracks: tensile stress concentration occurs at two sides of the dowel bar during load transfer [19, 21, 22]; due to low tensile strength of concrete, horizontal tensile cracks always develop at both sides of the dowel bar as shown in Fig. 1(b).
- Dowel bar corrosion: under repetitive loads, the external epoxy coating will show signs of wear, which then leads to the corrosion of steel as depicted in Fig. 1(c) [8, 13, 22-24].
- No free sliding: corrosion-induced dowel bar volume expansion and dowel bar misalignment will create lock-in stresses in concrete pavements. Therefore, as shown in Fig. 1(d), transverse cracks may initiate as moisture and temperature changes [2, 3, 25].

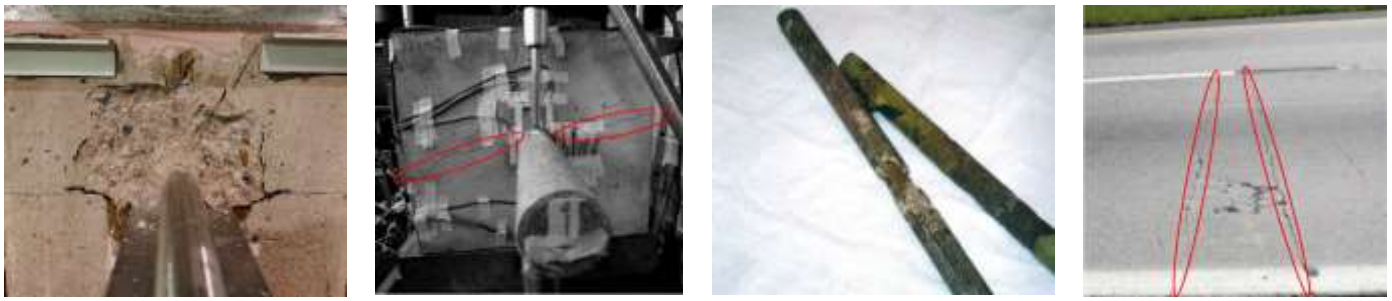

(a) (b) (c) (d)

Fig. 1. Critical issues of dowel bar applications (a) concrete crushing [19], (b) horizontal tensile cracks [26], (c) dowel bar corrosion [3], (d) transverse cracks [3].

In addition, corroded dowel bars will reduce the stiffness of concrete support and then impair load transfer ability between pavement slabs. For addressing this issue, corrosion-free materials like stainless steel and fibre-reinforced polymer (FRP) are adopted as potential alternatives to fabricate dowel bars [8, 9, 13, 16, 27, 28]. To mitigate concrete compressive stress concentration, traditional dowel bars can be replaced by elliptical and plate dowel bars that expand the contact area between concrete and steel [24, 29].

Furthermore, because of excellent durability of precast concrete units, individual precast slabs can be reused

to reduce the production of construction waste. In China, around 30 to 40 percent of municipal waste comes from construction and demolition waste [30]. Globally, the construction and demolition waste market is predicted to be USD 34.4 billion by 2026 [31]. Therefore, the main objective of this paper is to develop and test a demountable stainless steel bar connection system that promotes the reuse of PCP panels. Monotonic load tests and finite element analysis (FEA) were conducted to study the structural performance of concrete blocks employing the proposed connection system. Parameters including the stainless steel bar connection width, the stainless steel plate width, thickness and end distance were investigated. Based on the deformations of the stainless steel bar connection and high-strength bolts, an analytical approach was derived to predict the design load of the demountable stainless steel bar connection system. With the application of the collected test and FEA data, design recommendations are also proposed to instruct the connection design.

2. Design and materials

2.1. Design of connection

Fig. 2(a) shows the proposed demountable stainless steel bar connection system which consists of the stainless steel plate, stainless steel tube, stainless steel bar connection and high-strength bolts. Because of superior corrosion resistance, the application of stainless steel in component fabrication can extend the service life of the connection system. As high-strength bolts are replaceable, it is recommended to use 12.9 grade bolts to maximise the ultimate load of the connection system and observe the most critical failure mode. The main role of each component is introduced below:

- Stainless steel plate: bear (transfer) load from (to) the concrete block in load transfer.
- Stainless steel bar connection: achieve load transfer between adjacent pavement blocks.

- Stainless steel tube: create space for the installation of the stainless steel bar connection.
- High-strength bolts: connect the stainless steel bar connection to the stainless steel plate.

To accommodate the demountable stainless steel bar connection system, as shown in Fig. 2(b), two types of concrete blocks with a stainless steel tube or a stainless steel plate were prepared.

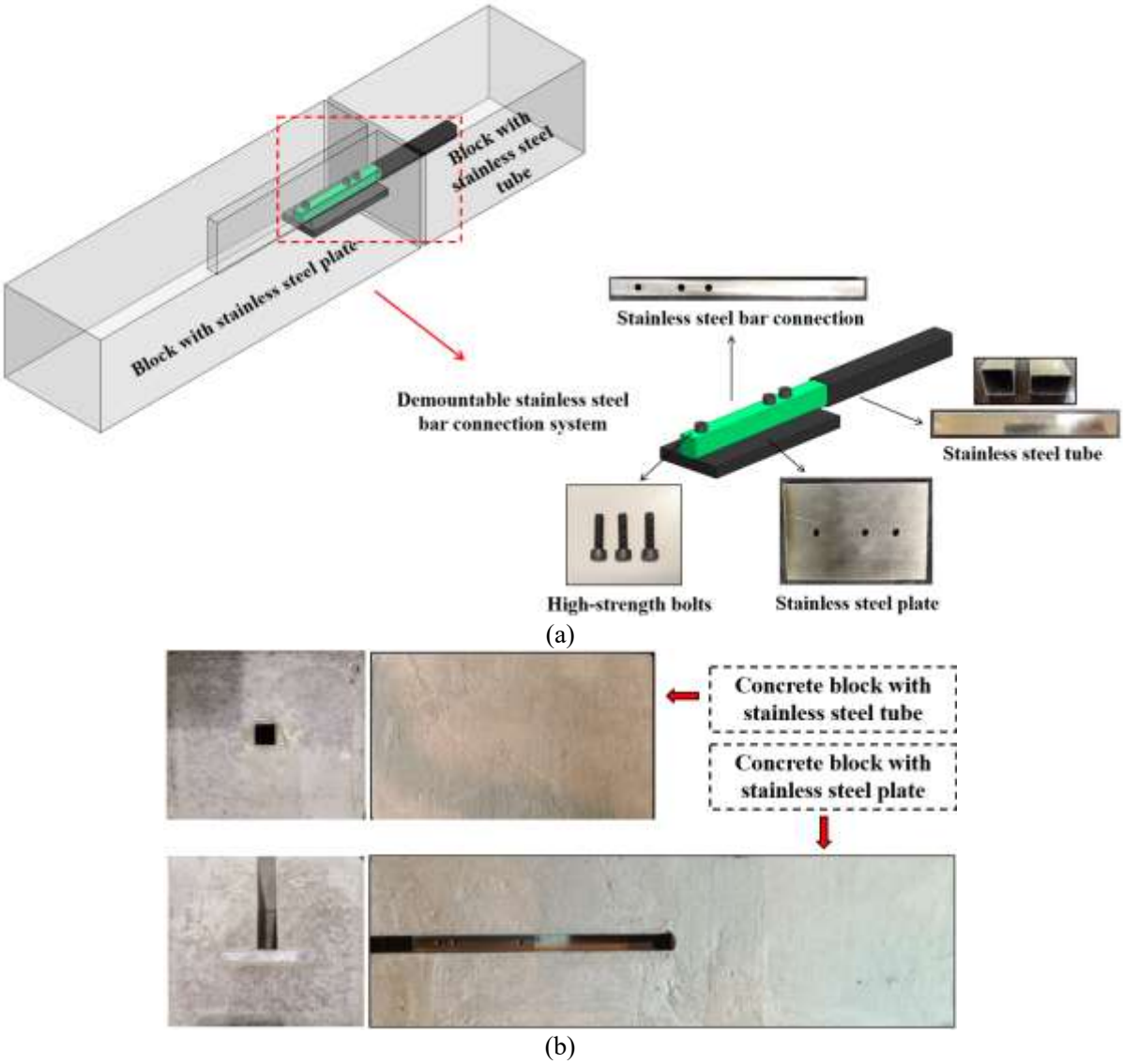

Fig. 2. Concrete blocks with demountable stainless steel bar connection system (a) configuration, (b) concrete blocks.

2.2. Assembly

Fig. 3 introduces the installation of this demountable pavement connection. In the first step, the stainless steel bar connection is inserted into the top concrete slot and then moved into the stainless steel tube embedded in the concrete block. After that, high-strength bolts are installed from the top slot to connect the

89 stainless steel bar connection and plate. The load transfer from the embedded plate to the stainless steel bar
90 connection is accomplished by the thread effect between high-strength bolts and threaded holes drilled in
91 the stainless steel plate. When it comes to replacing concrete pavement units, the stainless steel bar
92 connection can be dismantled after removing high-strength bolts. Compared with traditional dowel bars,
93 the demountable stainless steel bar connection system achieves flexible installation and disassembly of the
94 connection component. Therefore, discrete connections and individual precast pavement units can be reused.

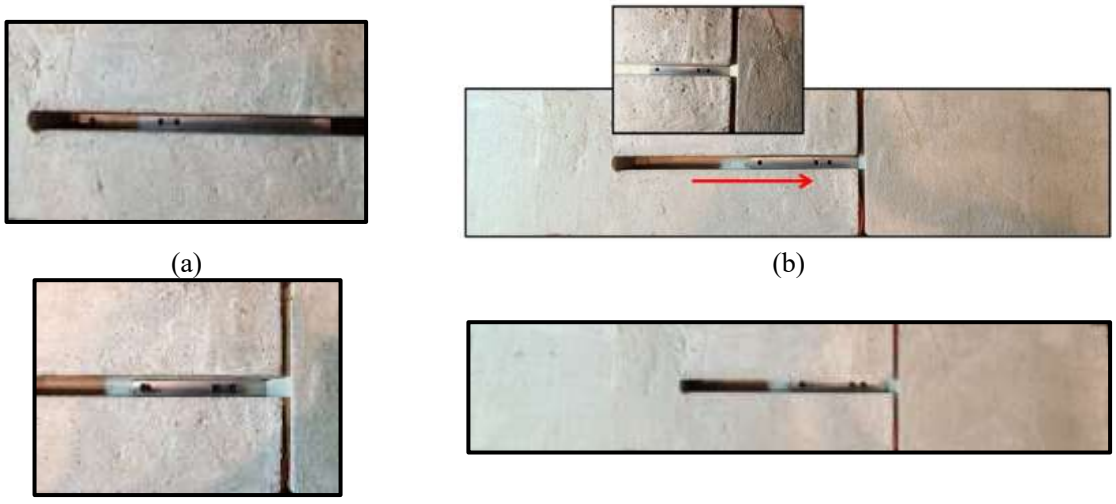

Fig. 3. Installation procedures (a) install connection into concrete slot, (b) move connection into embedded tube, (c) install high-strength bolts, (d) complete installation.

95 **2.3. Materials**

96 **2.3.1. Normal strength concrete**

97 Normal strength concrete (NSC) with a target cylinder compressive strength of 35 MPa was adopted to cast
98 concrete specimens and the corresponding mix proportions are listed in Table 1. At the beginning of
99 experimental tests, both cylinder compressive strength and splitting tensile strength of concrete were
100 measured following BS EN 12390-3 [32] and BS EN 12390-6 [33]. Table 2 summarises the obtained
101 concrete material properties including the cylinder compressive strength and splitting tensile strength.

102 Table 1 Mix proportions of normal strength concrete (kg/m^3).

Water	Cement	Sand	Aggregate
210	420	620	1150

Table 2 Material properties of normal strength concrete.

	Cylinder compressive strength (MPa)	Splitting tensile strength (MPa)
Average	34.45	3.59
CoV	0.02	0.04

2.3.2. Stainless steel

304 austenitic stainless steel was utilised to manufacture the components of the demountable stainless steel bar connection system. To acquire the material properties of the stainless steel plate and the stainless steel bar connection, tensile coupons were extracted from these components and designed according to BE EN ISO 6892-1 [34]. Fig. 4(a) shows the uniaxial tension test conducted by using the Instron 5982 electro-mechanical high force universal testing machine with a capacity of 100 kN. Strain gauges attached at both sides of the coupon were adopted to obtain the modulus of elasticity of stainless steel. The elongation of the coupon was acquired by the video extensometer at the left side of the tensile machine. Fig. 4(b) plots the full-range stress-strain curves of the stainless steel bar connection and plate. Related material properties determined from uniaxial tension tests are summarised in Table 3. Due to the size limitation of the tube specimens, the material properties provided by the manufacturer were adopted as listed in Table 4. Then the full stress-strain relationship of the stainless steel tube was predicted by Eqs. (1) to (3) proposed by Rasmussen [35], where, ε_n and σ_n are the nominal strain and the nominal stress, respectively; $\sigma_{0.01}$ and $\sigma_{0.2}$ are 0.01% and 0.2% proof stress, respectively; σ_u is the ultimate strength.

$$\varepsilon_n = \frac{\sigma_n}{E} + 0.002\left(\frac{\sigma_n}{\sigma_{0.2}}\right)^n,\ n = \frac{\ln(20)}{\ln(\sigma_{0.2}/\sigma_{0.01})}\ (\sigma_n \le \sigma_{0.2}) \tag{1}$$

$$\varepsilon_n = \frac{\sigma_n - \sigma_{0.2}}{E_{0.2}} + \varepsilon_u\left(\frac{\sigma_n - \sigma_{0.2}}{\sigma_u - \sigma_{0.2}}\right)^m,\ m = 1 + 3.5\frac{\sigma_{0.2}}{\sigma_u}\ (\sigma_n > \sigma_{0.2}) \tag{2}$$

$$E_{0.2} = \frac{E}{1 + 0.002n/e},\ e = \frac{\sigma_{0.2}}{E} \tag{3}$$

Table 3 Material properties of stainless steel plate and connection.

Stainless steel	Modulus of elasticity E (GPa)	Yield strength $\sigma_{0.2}$ (MPa)	Ultimate tensile strength σ_u (MPa)	Fracture strain ε_f

Stainless steel plate	192.5	405	789.7	0.529
Stainless steel bar connection	190.9	394	820.6	0.593

Table 4 Material properties of stainless steel tube.

Stainless steel	E (GPa)	$\sigma_{0.01}$ (MPa)	$\sigma_{0.2}$ (MPa)	σ_u (MPa)	ε_f
Stainless steel tube	190.0	220	320	650	0.43

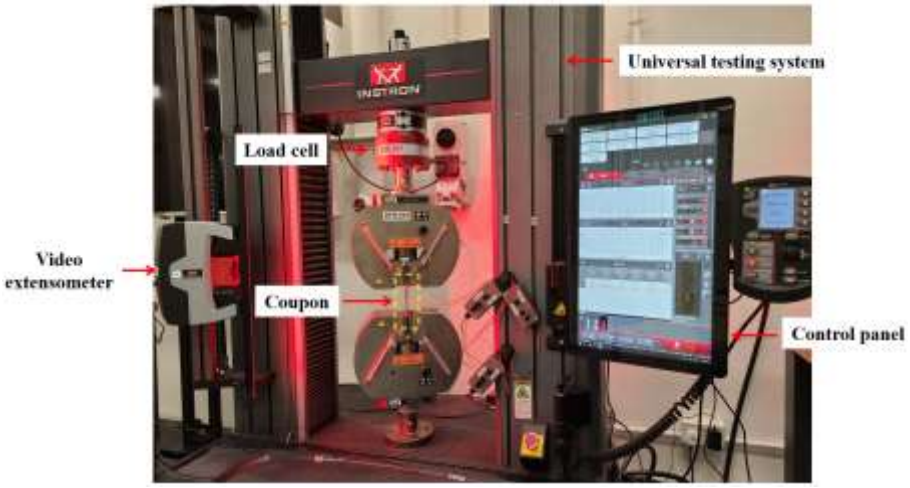

(a)

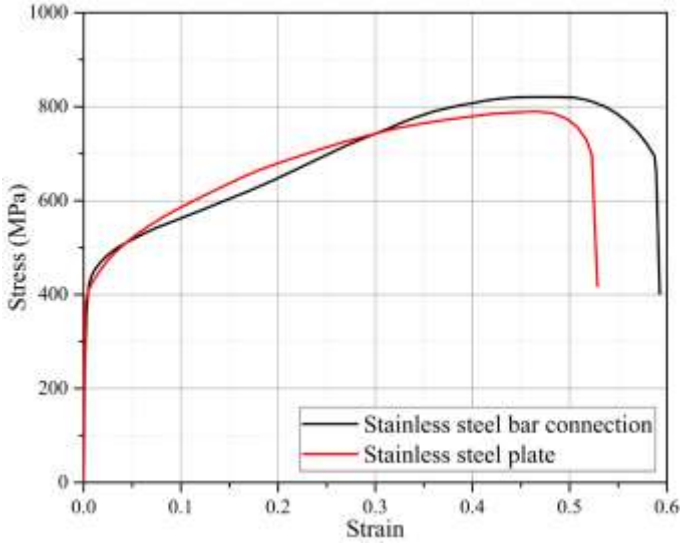

(b)

Fig. 4. Uniaxial tension tests of stainless steel (a) test setup, (b) stress-strain curve of stainless steel components.

2.3.3. High-strength bolt

12.9 grade high-strength bolts, with ultimate tensile strength exceeding 1200 MPa, were used to connect the stainless steel bar connection and plate. To assess the uniaxial tensile behaviour, circular coupons milled from bolt specimens were tested. Fig. 5 depicts the stress-strain curve of the 12.9 grade high-strength bolt. Relevant material properties obtained from uniaxial tension tests are summarised in Table 5.

Table 5 The material properties of 12.9 grade high-strength bolt.

Bolt grade	Modulus of elasticity E (GPa)	Yield strength $\sigma_{b,0.2}$ (MPa)	Ultimate tensile strength σ_{ub} (MPa)	Fracture strain ε_f
12.9	211.2	1179	1408	0.116

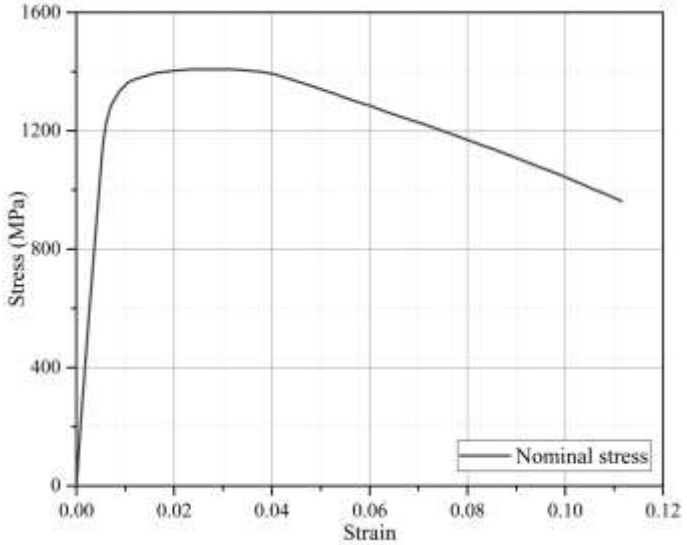

Fig. 5. The stress-strain relationship of 12.9 grade high-strength bolt.

3. Test methodology

3.1. Test specimens

To investigate the structural performance of concrete blocks with the demountable stainless steel bar connection system, parameters including the width of stainless steel bar connection, the width and the end distance of stainless steel plate were experimentally investigated. As the pavement joint failure generally initiates at the critical connection which transfers the largest load, it is reasonable to focus on the structural behaviour of an individual connection and conduct elemental tests [13, 24, 36-38].

In experimental tests, the width and height of the concrete blocks were 180 mm and 150 mm, respectively, which was proportional to the traditional dowel bar spacing and concrete pavement thickness considering a scale factor of 0.6. The lengths of the loaded block with the embedded stainless steel plate and the reaction block with the stainless steel tube were 600 mm and 300 mm, respectively. Regarding the stainless steel bar connection, the section area and the length of this component were determined from the standard dowel bar, equal to 289 mm^2 and 288 mm, respectively, after considering the scale factor. The joint width between

concrete blocks was set to 8 mm following the maximum design requirement [3]. Fig. 6(a) shows the dimension of two stainless steel bar connections, in which w_s, h_s, and l represent the width, height and the length of the connection, respectively. Three bolt holes were drilled in the connection to install M6 high-strength bolts. The configuration of the stainless steel plate and the assembled connection and plate are displayed in Fig. 6(b) and 6(c), respectively. High-strength bolts B1 and B2 near the joint surface are utilised to take the vertical load and the bolt B3 is installed to fix the location of the stainless steel bar connection. Because the stainless steel plate width and the end distance e_1 between the first bolt and the pavement joint surface may affect the behaviour of the connection, following design recommendations in Eurocode 1993-1-8 [39], the end distance e_1 was considered to be 15 mm or 30 mm, and the width of the stainless steel plate varied from 40 mm to 80 mm. The end distance between the bolt B3 and the end of the plate was fixed at 15 mm in all specimens. To accommodate different stainless steel bar connections in the reaction block, two types of stainless steel tubes with a thickness of 1 mm and a length of 150 mm were used as depicted in Fig. 6(d).

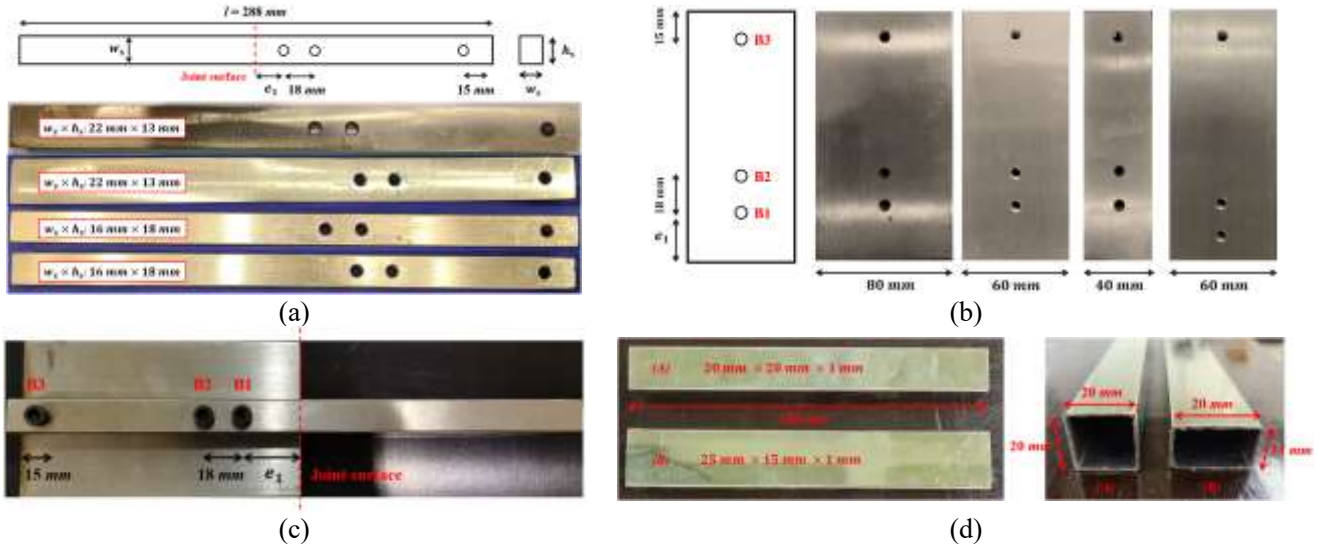

Fig. 6. Dimensions of demountable stainless steel bar connection system (a) stainless steel bar connection, (b) stainless steel plate, (c) assembled plate and connection (d) stainless steel tube.

3.2. Test setup

In experimental tests, 10 specimens were prepared and tested. Table 6 summarises the corresponding test matrix, where W and N denote the wide-section (22 mm × 13 mm) and the narrow-section (16 mm × 18 mm) connections, respectively; E represents the steel plate end distance e_1. Each specimen was specified by "connection type, stainless steel plate width and end distance e_1". Taking "N60E15" as an instance, this specimen employs a narrow-section connection and a stainless steel plate with a width of 60 mm and an end distance e_1 of 15 mm. Fig. 7(a) and 7(b) display the configuration of test specimens and the corresponding test setup. Each specimen consisted of the reaction block with the stainless steel tube, the loaded block with the stainless steel plate and the stainless steel bar connection with high-strength bolts. The main purpose of experimental tests was to investigate the shear capacity of the demountable stainless steel bar connection system. Pavement subbase was not considered because this layer only affected the vertical load transferred to the adjacent slab while had no influence on the shear capacity of an individual connection. To avoid unexpected upward deformation under vertical load, the reaction block was tightened to the rigid support by a fixing device. The loaded block was supported by a roller placed 500 mm from the pavement joint surface. Regarding the load arrangement, the vertical load was applied by a hand pump to a steel block placed close to the pavement joint surface and recorded by a load cell with a capacity of 100 kN installed between the loading head and the steel block. The loading rate was manually controlled at around 0.3 mm per minute. Fig. 7(c) shows test instrumentations to measure the vertical deflection of the loaded block and the stain development in concrete and steel. Two linear variable displacement transducers (LVDTs) with a range of 25 mm and an accuracy of 0.001 mm were placed at both sides of the loaded block and the averaged displacement measurement was taken as the deflection of the specimen. Strain gauges

177 LS-1, LS-2 and RS-1 with a gauge length of 10 mm were attached to the loaded and the reaction blocks to
178 evaluate the compressive strain development of concrete. The strain development in the stainless steel bar
179 connection was assessed by 5 mm long strain gauges SS-1 to SS-3 affixed close to the bolt holes. Both the
180 deflection and strain data were obtained via a Kyowa data logger USB-70B-30 with a data gathering rate
181 at 1 Hz.

182 Table 6 Test matrix of stainless steel bar connection system.

Specimen ID	Connection type	Connection width (mm)	Connection height (mm)	Steel plate width (mm)	End distance (mm)
N40E15	Narrow	16.04	17.93	40	15
N40E30	Narrow	16.02	17.90	40	30
N60E15	Narrow	15.98	17.95	60	15
N60E30	Narrow	16.03	17.92	60	30
N80E15	Narrow	16.05	17.93	80	15
N80E30	Narrow	15.99	17.95	80	30
W60E15	Wide	22.07	12.92	60	15
W60E30	Wide	22.04	12.95	60	30
W80E15	Wide	22.03	12.94	80	15
W80E30	Wide	22.05	12.93	80	30

183

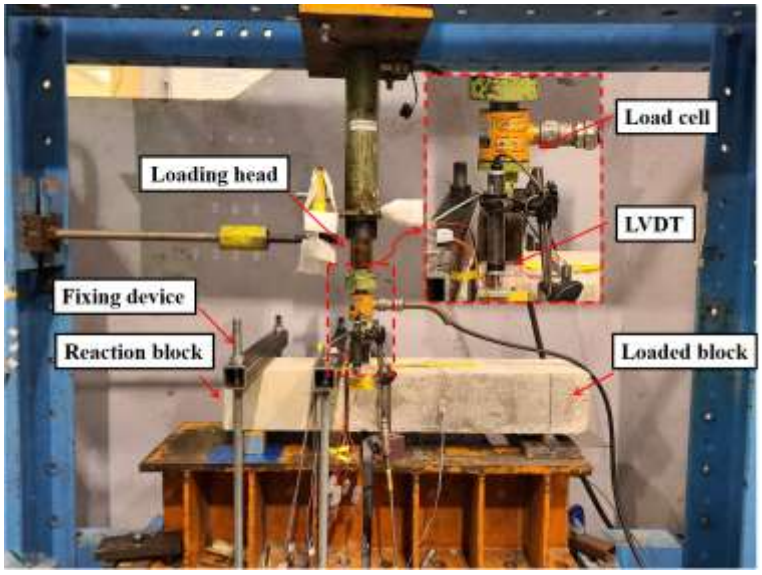

(a)

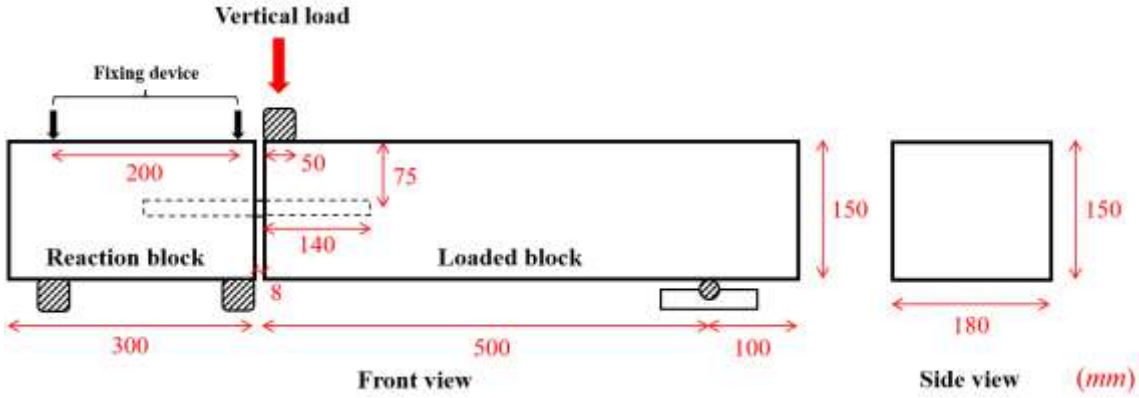

(b)

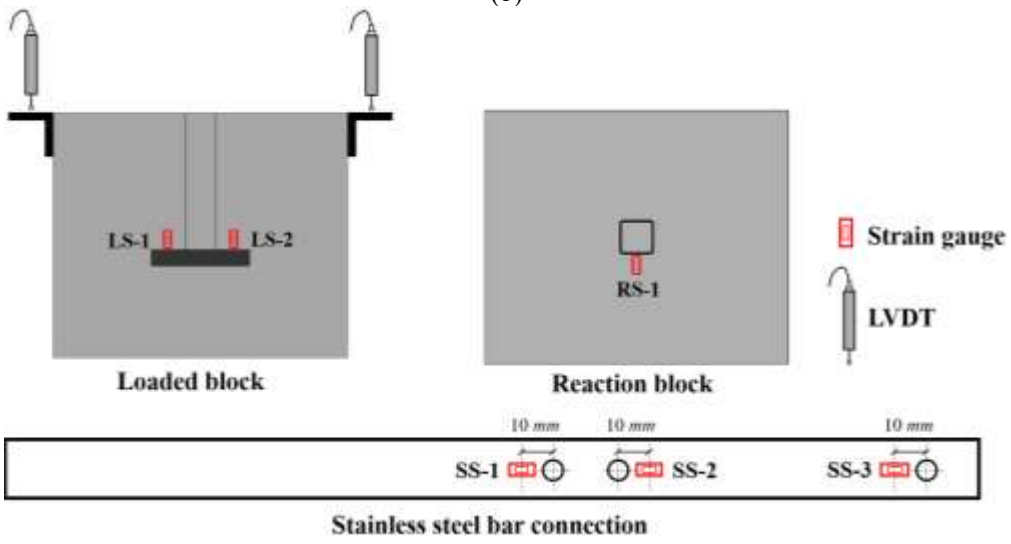

(c)

Fig. 7. Test setup and instrumentations (a) actual test setup, (b) test setup (schematic view) (c) test instrumentations.

4. Results and discussion

4.1. Failure modes

Two typical failures were observed in experimental tests. Firstly, due to concrete compressive stress concentration, severe concrete crushing was observed under the stainless steel tube in the reaction block as shown in Fig. 8. Although the application of the wide-section connection could expand the contact area between concrete and steel, localised concrete crushing was still severe at the end of experimental tests. However, because a large contact area was created by the stainless steel plate, no concrete crushing failure was found in the loaded concrete block. The other typical failure observed in specimens with the demountable stainless steel bar connection system was bolt fracture. As the vertical load increased, large

193 flexural and shear deformations were created in the stainless steel bar connection. Therefore, the relative
194 deformation between the stainless steel bar connection and plate was increased, resulting in great axial
195 loads created in the high-strength bolts B1 and B2 near the joint surface. Once the fracture strain of high-
196 strength bolts was reached, brittle bolt fracture occurred at the end of experimental tests as captured in Fig.
197 9.

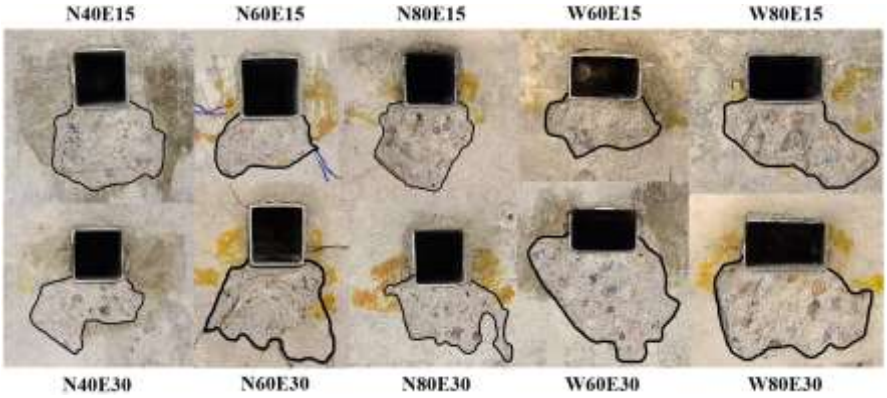

Fig. 8. Localised concrete crushing in the reaction block.

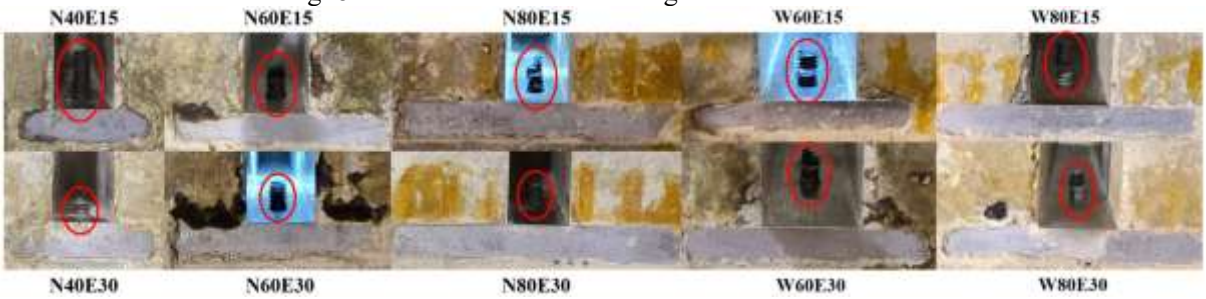

Fig. 9. Bolt fractures in the loaded concrete block.

198 **4.2. Deflection response**

199 In experimental tests, the vertical deflection of the loaded block was specified as the average displacement
200 recorded by two LVDTs. Fig. 10 plots the load-deflection curves of tested specimens. Due to lower flexural
201 stiffness, wide-section connections normally experienced larger flexural deformation compared with
202 narrow-section counterparts as the vertical load increased. Therefore, the initial stiffness of specimens,
203 namely the tangential slope of the load-deflection curve, was significantly reduced. In addition, as can be
204 seen in Fig. 11, stainless steel bar connections with a 30 mm end distance were subjected to additional
205 flexural deformation in contrast to connections with a 15 mm end distance. Therefore, lower initial stiffness

206 was caused as presented in Fig. 10. In terms of high-strength bolts, locations of bolts in each connection
207 were marked by blue lines as shown in Fig. 11. After increasing the end distance of the stainless steel plate
208 to 30 mm, the axial force development in the first bolt B1 was accelerated, while the bolt load evolution in
209 the second bolt B2 was limited. As a result, the ultimate load of specimens was impaired before bolt fracture.
210 However, since no concrete crushing failure was observed in the loaded block, the width of the stainless
211 steel plate had limited effects on the initial stiffness and ultimate load of test specimens.

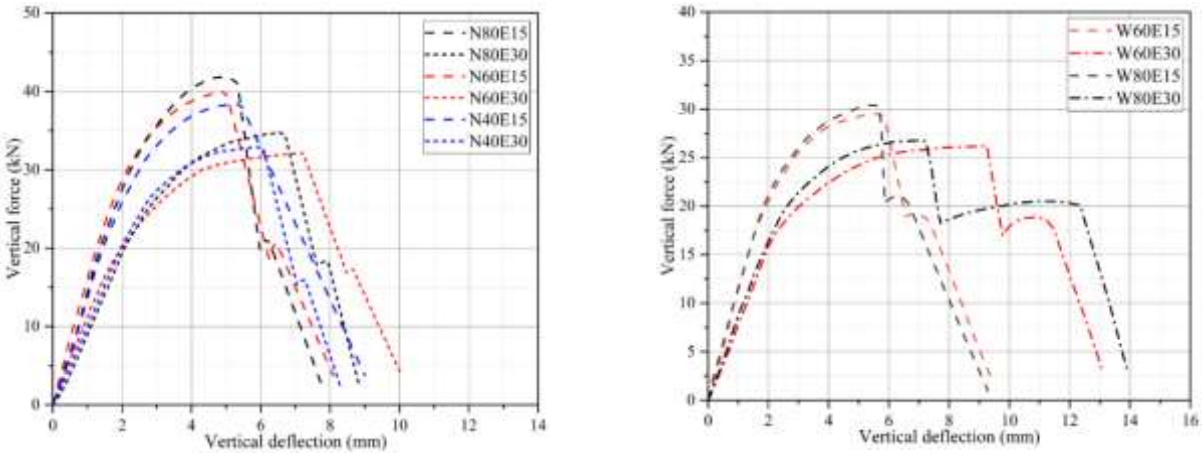

(a) (b)

Fig. 10. Load-deflection curves of specimens with demountable stainless steel bar connection system (a) narrow-section connection, (b) wide-section connection.

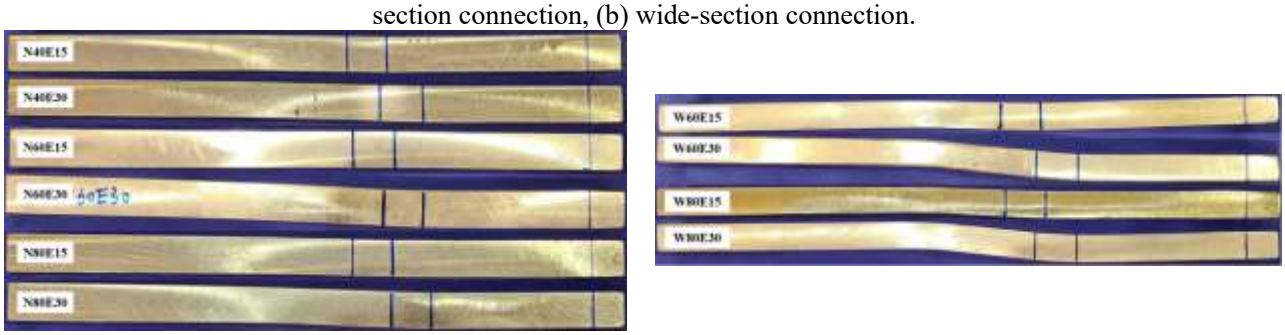

(a) (b)

Fig. 11. Deformed stainless steel bar connections (a) narrow-section connection, (b) wide-section connection.

212 **4.3. Concrete strain development**

213 The development of concrete compressive strain at the joint surface of the loaded block is plotted in Fig.
214 12(a) and 12(b). In contrast to specimens with a 30 mm end distance, although larger compressive strains
215 were developed in specimens with a 15 mm end distance, the recorded maximum strain was far from the
216 crushing strain of concrete. However, because of the limited contact area between concrete and the stainless

217 steel tube, the strain development in the reaction block exhibited a different trend, which was recorded by
218 the strain gauge RS-1 in each specimen as plotted in Fig. 12(c) and 12(d). As the vertical load increased,
219 the occurrences of strain reduction and nonlinearity indicated the initiation of localised concrete crushing.
220 To study the effect of compressive stress concentration in the reaction block, the development of concrete
221 compressive strain under the stainless steel tube was evaluated. As the vertical load increased, the rate of
222 strain development was represented by the inverse of the slope of the load-strain curve. For each specimen,
223 the strain development rate during the ascending stage was determined by linear regression analysis. The
224 average compressive strain development rate for specimens with the narrow-section connection was
225 2.94×10^{-4} /kN. While for the wide-section connection cases, with an expanded contact area, this value was
226 reduced by up to 29 percent and equal to 2.08×10^{-4} /kN. However, in spite of mitigating compressive stress
227 concentration, the ultimate of specimens with the wide-section connection was reduced by more than 19
228 percent compared with the narrow-section connection cases.

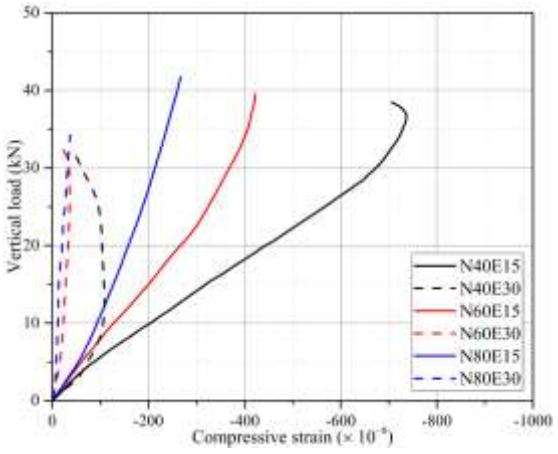

(a)

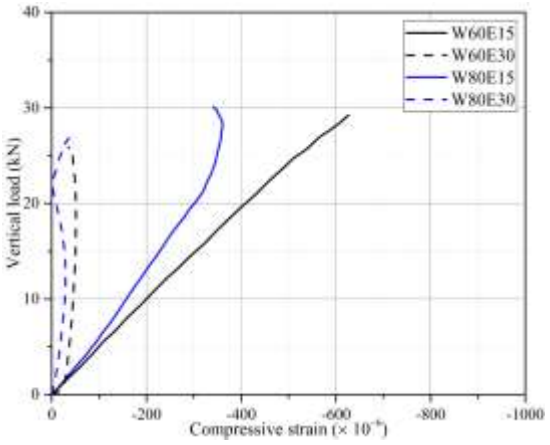

(b)

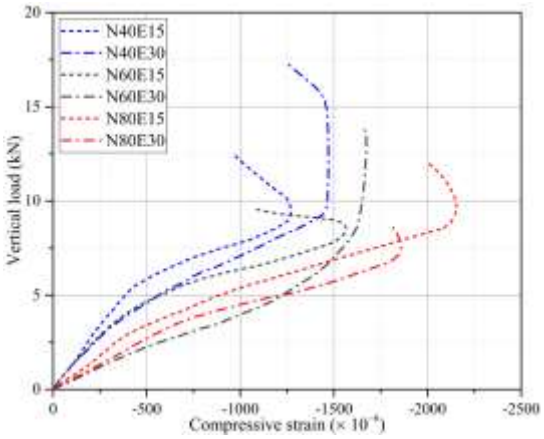

(c)

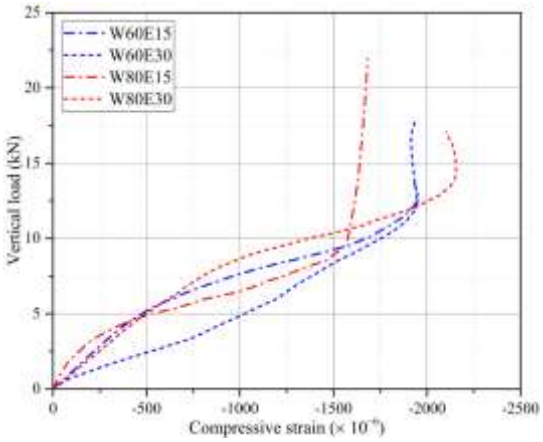

(d)

Fig. 12. Strain development in concrete blocks (a) narrow-section connection loaded block, (b) wide-section connection loaded block, (c) narrow-section connection reaction block, (d) wide-section connection reaction block.

4.4. Steel strain development

Under vertical load, the stainless steel bar connection was subjected to large flexural deformation during load transfer. Three strain gauges SS-1 to SS-3 were attached on the top surface of the stainless steel bar connection to evaluate strain developments near bolt locations. According to the obtained strain data, the maximum flexural strain occurred near the second bolt and Fig. 13 displays the corresponding strain development with the increased vertical load. As the end distance of the stainless steel plate increased, the stainless steel bar connection was subjected to additional flexural deformation, thereby resulting in a high strain development rate. However, concrete crushing in the reaction block was still the dominant failure because the deformation of the connection remained elastic at the onset of concrete crushing.

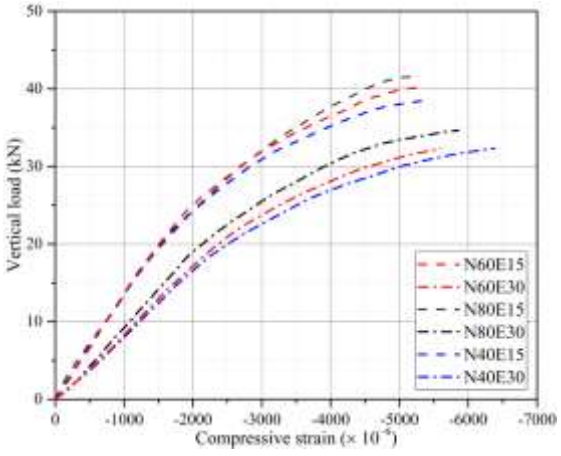

(a)

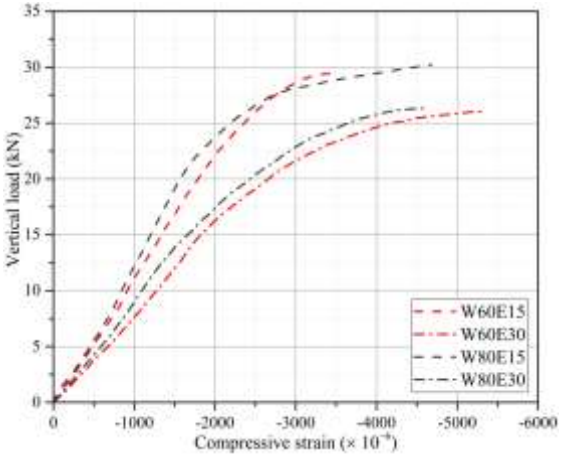

(b)

Fig. 13. Strain developments in stainless steel bar connections (a) SS-2 in narrow-section connection, (b) SS-2 in wide-section connection.

5. Updated connection system

5.1. Design of updated connection

According to test results, the application of the demountable stainless steel bar connection system cannot achieve a high ultimate load with low compressive stress concentration. As a result, to further expand the contact area between concrete and steel, the stainless steel tube in the reaction block was replaced by the same stainless steel plate as applied in the loaded block. Fig. 14(a) and 14(b) show the configurations of the updated stainless steel bar connection system with and without concrete. Three slotted holes that allowed sliding of concrete blocks were drilled to connect the stainless steel bar connection and plate in the reaction block. The dimension of the updated stainless steel bar connection is described in Fig. 14(c). Four specimens with the updated stainless steel bar connection system were tested and the corresponding test matrix is listed in Table 7.

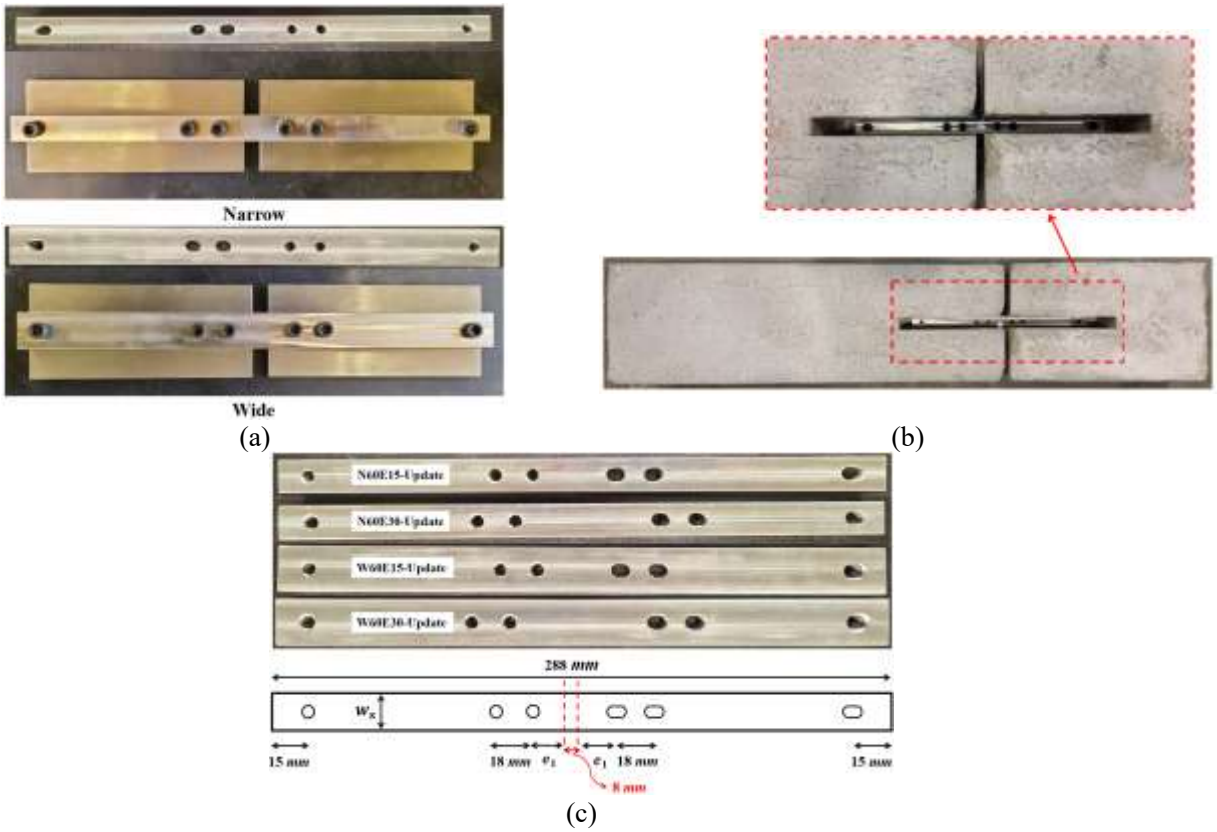

Fig. 14. Updated stainless steel bar connection system (a) configuration (without concrete), (b) configuration (with concrete), (c) dimension.

Table 7 Test matrix of updated stainless steel bar connection system.

Specimen ID	Connection type	Connection width (mm)	Connection height (mm)	Steel plate width (mm)	End distance (mm)
N60E15-Update	Narrow	16.03	17.97	60	15
N60E30-Update	Narrow	16.01	17.95	60	30
W60E15-Update	Wide	22.02	12.95	60	15
W60E30-Update	Wide	22.02	12.98	60	30

5.2. Failure modes and deflection response

Bolt fracture and localised concrete crushing were still found in specimens with the updated connection system at the end of experimental tests as shown in Fig. 15. However, after replacing the stainless steel tube by an embedded plate in the reaction block, the contact area between concrete and steel was expanded and the support stiffness of the reaction block was enhanced. As a result, both the initial stiffness and ultimate load of specimens with the updated connection system were improved as verified in Fig. 16.

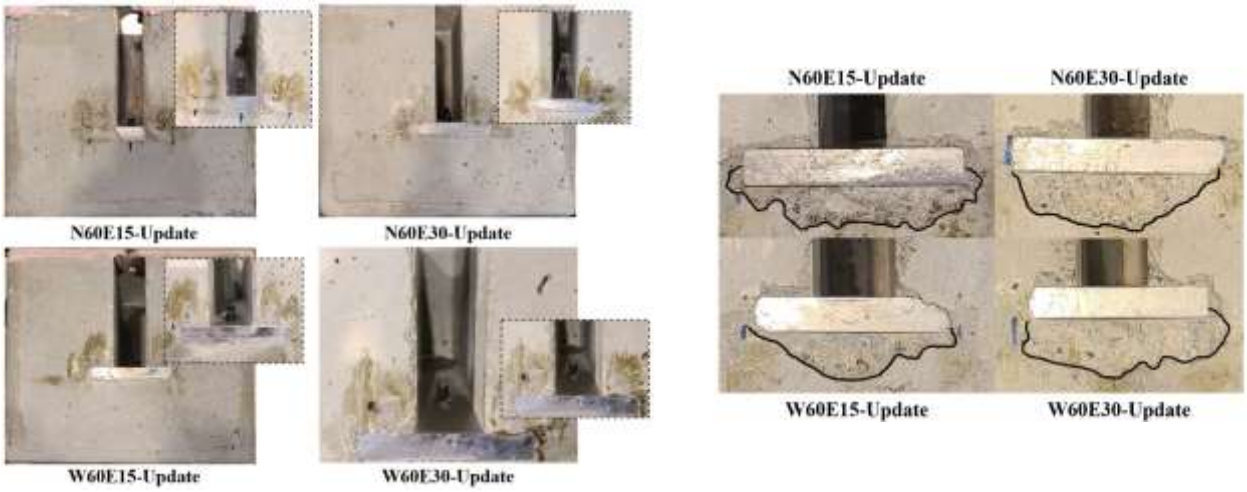

(a) (b)

Fig. 15. Bolt fracture and concrete crushing (a) bolt fracture, (b) concrete crushing.

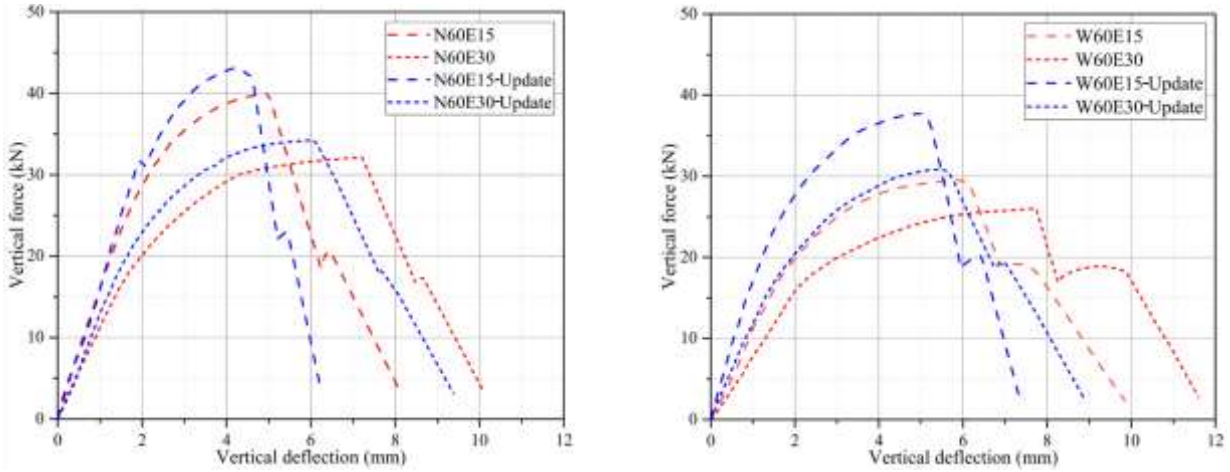

(a) (b)

Fig. 16. Load-deflection curves of specimens with updated connection system (a) updated narrow-section connection, (b) updated wide-section connection.

5.3. Strain development in concrete

As the main purpose of updating the stainless steel bar connection system was relieving compressive stress concentration, concrete strain development under the stainless steel plate of the reaction block was assessed as plotted in Fig. 17. The recorded strain data indicated that localised concrete crushing under the stainless steel plate initiated at around 15 kN. The strain development rates of specimens with the updated narrow-section and wide-section connections were 8.33×10^{-5} /kN and 8.92×10^{-5} /kN, respectively. Compared with the reaction block with the stainless steel tube, the strain localisation effect was mitigated by up to 71 percent after replacing the embedded tube by a stainless steel plate. Furthermore, it was found that the width of connection had limited influence on the development of compressive strain in concrete because the contact area between concrete and steel was affected by the stainless steel plate width. As a result, the updated narrow-section connection system was recommended to achieve high initial stiffness with low compressive stress concentration.

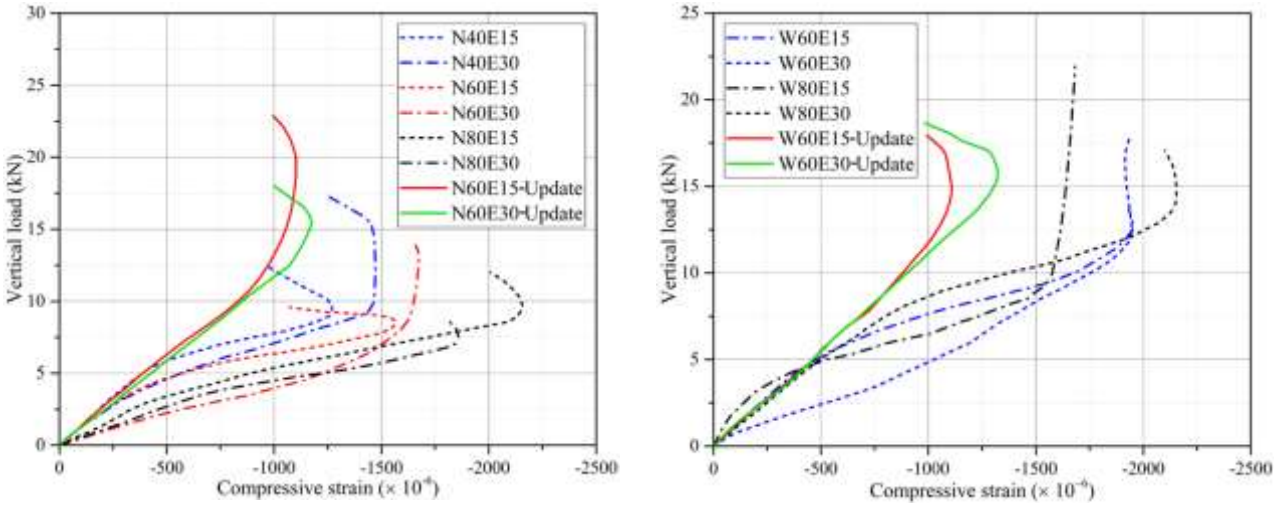

(a) (b)

Fig. 17. Strain developments in reaction blocks with stainless steel plate (a) narrow-section connection, (b) wide-section connection.

6. Finite element analysis

Through the application of the ABAQUS explicit solver [40], finite element models with the demountable stainless steel bar connection system were developed and validated against test results. The extended parametric analysis was then conducted to further investigate factors that affected the structural performance of the updated narrow-section stainless steel bar connection system.

6.1. Finite element model

The components of developed models were simulated by three-dimensional solid elements with reduced integration (C3D8R) as shown in Fig. 18. After carrying out the meshing sensitivity analysis, the minimum mesh size of concrete around the pavement connection at the joint surface was set to 4 mm to precisely capture localised crushing failure. However, for the region away from the joint surface, the mesh size was increased to 20 mm to reduce the computational effort. For stainless steel components, the mesh size of 4 mm was adopted to simulate the induced flexural and shear deformation under vertical load. Because high-strength bolts were critical components that governed the ultimate load of test specimens, the mesh size along the bolt shank was adjusted to 0.5 mm to model brittle fracture failure.

The contact behaviour between different components was simulated by contact pairs with the normal and tangential contact behaviour modelled by the "hard" contact and the "penalty" friction formulation, respectively. The frictional coefficient between concrete and steel was 0.35 as suggested by Al-Humeidawi et al. [41]. Boundary conditions and the load arrangement in FEA followed those in experimental tests. As shown in Fig. 19(a), the bottom surface of the reaction block was completely restricted. The roller support was simplified by a coupling constraint as depicted in Fig. 19(b). Because the loaded block beyond the roller had no influence on the performance of the whole system, this part was neglected in FEA. Fig. 19(c) introduces a displacement-type vertical load applied via a coupling constraint. As thread stripping failure was not observed in experimental tests, the threaded bolt shank was simplified with the net section area A_0 equal to 20.1 mm^2 for M6 bolts according to EN ISO 898-1 [42]. This simplification was verified by Li et al. [43] and the thread gripping effect was modelled by a tie constraint as stressed in Fig. 19(d).

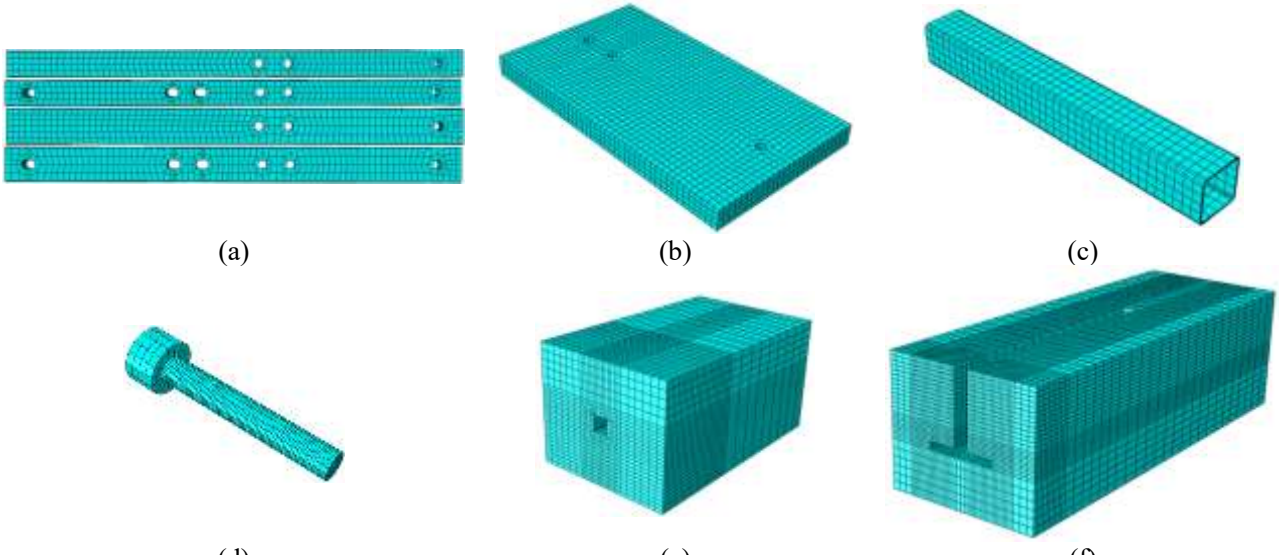

Fig. 18. Finite element model (a) stainless steel bar connection, (b) stainless steel plate, (c) stainless steel tube, (d) high-strength bolt, (e) concrete block (stainless steel tube), (f) concrete block (stainless steel plate).

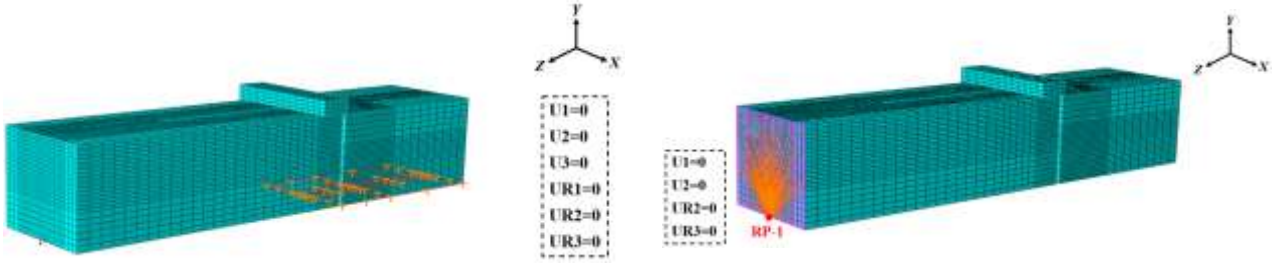

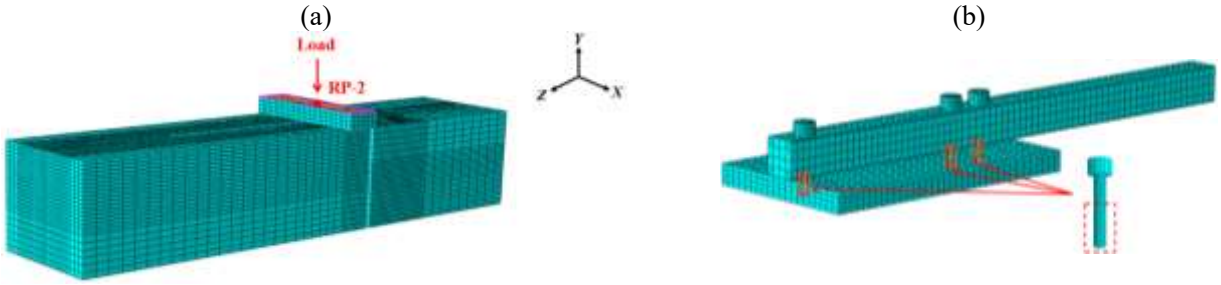

Fig. 19. Boundary conditions and constraints in finite element analysis (FEA) (a) fixed reaction block, (b) roller support simulation, (c) load arrangement, (d) thread effect.

6.2. Material modelling

6.2.1. Concrete

The concrete damaged plasticity (CDP) model proposed by Lubliner et al. [44] and modified by Lee et al. [45] was used to model the behaviour of concrete. Regarding the uniaxial compressive behaviour, the linear stress-strain relationship was defined before $0.4f_c$ as expressed in Eq. (4), where, σ_c and ε_c denote the compressive stress and strain, respectively; f_c is the uniaxial compressive strength of concrete; E_c is the scant modulus of elasticity at $0.4f_c$. For the nonlinear plastic stage, before reaching the limited compressive strain $\varepsilon_{c,lim}$ at $0.5f_c$ within the softening branch, Eq. (5) recommended in CEB-FIP Model Code 2010 was adopted [46]. For the descending stage beyond $\varepsilon_{c,lim}$, Eqs. (6) and (7) proposed in CEB-FIP Model Code 1990 were selected [47], where, ε_{cl} is the strain at the maximum compressive stress; E_{ci} is the tangential modulus of elasticity at the origin; E_{cl} is the scant modulus at the compressive strength; k is the plasticity number. Obtained material properties are summarised in Table 8.

$$\sigma_c = E_c \varepsilon_c \tag{4}$$

$$\frac{\sigma_c}{f_c} = \left[\frac{k\eta - \eta^2}{1+(k-2)\eta}\right], \eta = \left(\frac{\varepsilon_c}{\varepsilon_{cl}}\right), k = \left(\frac{E_{ci}}{E_{cl}}\right) \tag{5}$$

$$\sigma_c = \left[\left(\frac{1}{\frac{\varepsilon_{c,lim}}{\varepsilon_{cl}}}\xi - \frac{2}{(\frac{\varepsilon_{c,lim}}{\varepsilon_{cl}})^2}\right)\left(\frac{\varepsilon_c}{\varepsilon_{cl}}\right)^2 + \left(\frac{4}{\frac{\varepsilon_{c,lim}}{\varepsilon_{cl}}} - \xi\right)\left(\frac{\varepsilon_c}{\varepsilon_{cl}}\right)\right]^{-1} f_c \tag{6}$$

309
$$\xi = \frac{4\left[(\frac{\varepsilon_{c,lim}}{\varepsilon_{cl}})^2 \left(\frac{E_{ci}}{E_{cl}} - 2 \right) + 2\frac{\varepsilon_{c,lim}}{\varepsilon_{cl}} - \frac{E_{ci}}{E_{cl}} \right]}{\left[\frac{\varepsilon_{c,lim}}{\varepsilon_{cl}} \left(\frac{E_{ci}}{E_{cl}} - 2 \right) + 1 \right]^2} \quad (7)$$

310 In terms of tensile behaviour of concrete, a linear stress-strain relationship was defined before reaching the
311 uniaxial tensile strength of concrete as expressed by Eq. (8). For the descending stage, the bilinear stress-
312 crack width relationship suggested in CEB-FIP Model Code 2010 [46] was used as expressed by Eqs. (9)
313 to (11), where, ε_{ct} and σ_{ct} are the concrete tensile strain and stress, respectively; f_{ct} is the uniaxial tensile
314 strength of concrete; G_F is the fracture energy; w_t and w_c refer to the transition crack width and crack
315 opening width, respectively. Material properties related to uniaxial tensile behaviour of concrete are
316 tabulated in Table 9.

317
$$\sigma_{ct} = E_c \varepsilon_{ct} \quad (8)$$

318
$$\sigma_{ct} = f_{ct}\left(1.0 - 0.8\frac{w}{w_t}\right)(w \le w_t) \quad (9)$$

319
$$\sigma_{ct} = f_{ct}\left(0.25 - 0.05\frac{w}{w_t}\right)(w_t < w \le w_c) \quad (10)$$

320
$$G_F = 0.73 f_c^{0.18}, w_t = \frac{G_F}{f_{ct}}, w_c = \frac{5G_F}{f_{ct}} \quad (11)$$

321 Table 8 Concrete material parameters (uniaxial compression).

f_c (MPa)	ε_{cl}	E_{ci} (GPa)	E_{cl} (GPa)	E_c (GPa)	k
34.45	0.0024	29.6	14.4	26.2	2.06

322 Table 9 Concrete material parameters (uniaxial tension).

f_{ct} (MPa)	G_F (N/mm)	w_t (mm)	w_c (mm)
3.49	0.138	0.0396	0.198

323 In the CDP model, compressive and tensile damage variables d_c and d_t were incorporated. Birtel et al. [48]
324 indicated that the concrete compressive damage variable d_c increased as plastic strain accumulated and
325 could be calculated through Eq. (12). For the tensile damage variable of concrete d_t, it was proportional to

326 the required energy to form microcracks and Eqs. (13) and (14) were derived to determine d_t. Other
327 parameters including the dilation angle ψ, the equibiaxial compressive stress to uniaxial compressive stress
328 ratio f_{b0}/f_c, the tensile meridian to compressive meridian K, the eccentricity ε and the viscosity parameter
329 were obtained from the ABAQUS user's guide [49], equal to 38°, 1.16, 0.667, 0.1 as well as zero,
330 respectively.

331 $$d_c = 1 - \frac{\sigma_c E_c^{-1}}{\varepsilon_c^{pl}\left(\frac{1}{b_c} - 1\right) + \sigma_c E_c^{-1}}, b_c = 0.7, \varepsilon_c^{pl} = b_c \varepsilon_c^{in} \quad (12)$$

332 $$d_t = \frac{f_t\left(w - 0.4\frac{w^2}{w_t}\right)}{G_F}, w \le w_t \quad (13)$$

333 $$d_t = 1 - \frac{\left[f_t\left(0.125 - 0.025\frac{w}{w_t}\right)\left(w_c - w\right)\right]}{G_F}, w_t < w \le w_c \quad (14)$$

334 **6.2.2. Stainless steel**

335 The nominal stress-strain relationship of stainless steel was obtained from the coupon test data shown in
336 Fig. 4 or according to the material properties provided by the manufacturer as summarised in Table 4. The
337 true stress-strain curves were transferred from the nominal stress-strain curves by the converted equations
338 as expressed by Eqs. (15) and (16). Fig. 20 plots the true stress-strain curves of the stainless steel
339 components.

340 $$\sigma_t = \sigma_n\left(1 + \varepsilon_n\right) \quad (15)$$

341 $$\varepsilon_t = \ln\left(1 + \varepsilon_n\right) \quad (16)$$

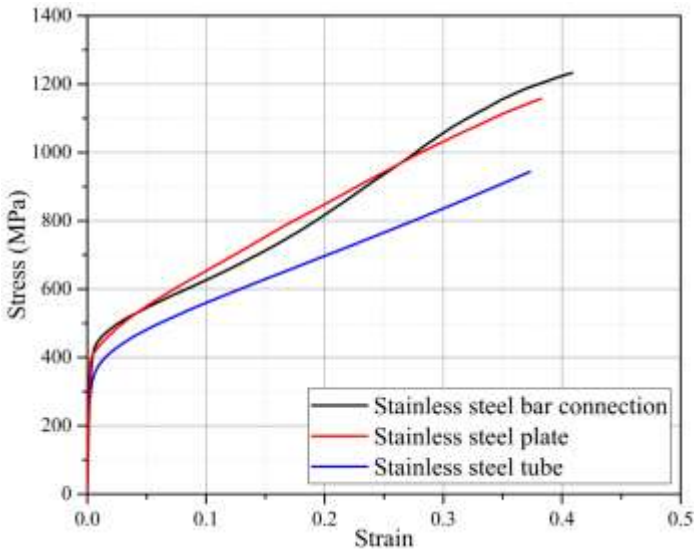

Fig. 20. True stress-strain curves of stainless steel.

6.2.3. High-strength bolt

Although the full-range stress-strain curve of 12.9 grade high-strength bolts was obtained via coupon tests, the post-necking true stress-strain relationship cannot be directly measured as the deformation within the necking zone was extermely non-uniform. Therefore, according to the bolt fracture simulation conducted by Yang et al. [50, 51], the post-necking stress-strain curve could be described with an exponential relationship as expressed by Eq. (17), where, $K=\sigma_{t,u}/n^n$, $n=\varepsilon_{t,u}$, $\sigma_{t,u}$ and $\varepsilon_{t,u}$ are the true stress and the true strain at the initiation of necking, respectively. Fig. 21 plots the derived stress-strain curve of 12.9 grade high-strength bolts. The pre-necking and post-necking stress-strain curves were adopted in FEA to simulate the behaviour of high-strength bolts.

$$\sigma_t = K\varepsilon_t^n \quad (17)$$

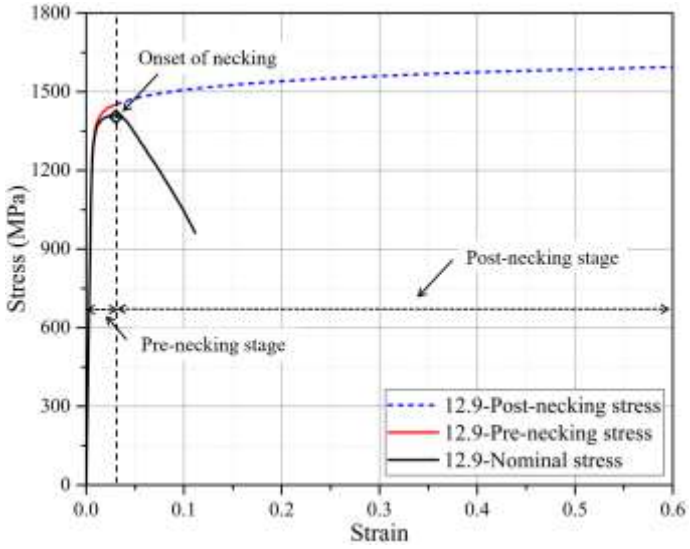

Fig. 21. Pre-necking and post-necking stress-strain curves of 12.9 grade high-strength bolt.

6.3. Fracture criterion

ABAQUS is capable of modeling steel fracture by using the ductile damage model. Bao and Wierzbicki [52, 53] carried out a series of experimental tests to investigate compressive, tensile and shear behaviour of aluminum alloy. The BW fracture criterion was then propsoed to define the relationship between the equivalent plastic strain (PEEQ) and the stress triaxiality as expressed by Eq. (18) [52, 53], where, η represents the stress triaxiality, η_0 is the stress triaxiality under uniaxial tension equal to 1/3; C_1 and C_2 are two material constants related to shear and tensile fracture behaviour, respectively.

$$\varepsilon_f(\eta)=\begin{cases}\infty \ (\eta<-\dfrac{1}{3})\\ \dfrac{C_1}{3\eta+1} \ (-\dfrac{1}{3}\le\eta<0)\\ (C_2-C_1)\left(\dfrac{\eta}{\eta_0}\right)^2+C_1 \ (0\le\eta<\eta_0)\\ \dfrac{C_2}{\eta/\eta_0} \ (\eta\ge\eta_0)\end{cases} \tag{18}$$

Although the BW fracture criterion was proposed based on test results of aluminum alloy, this criterion was also applicable in the modeling of bolt fracture after calibrations of C_1 and C_2 [50, 51]. From the research conducted by Li et al. [43], C_1 was 0.13 for 12.9 grade high-strength bolts. After comparing FEA results

with experimental test data, C_2 was then adjusted to 0.52. Regarding the damage evolution, it was defined by the displacement type with the linear softening law. A minimal displacement of 0.01 mm was adopted to achieve a sudden fracture after fracture initiation [50, 51].

6.4. Model validation

Localised concrete crushing and bolt fracture were two main failure modes observed in experimental tests. In FEA, crushing zones in reaction blocks were well simulated by the concrete compressive damage variable as shown Fig. 22. With the application of the BW fracture criterion, Fig. 23 depicts bolt fracture failure predicted in FEA, which closely aligns with those observed in experimental tests.

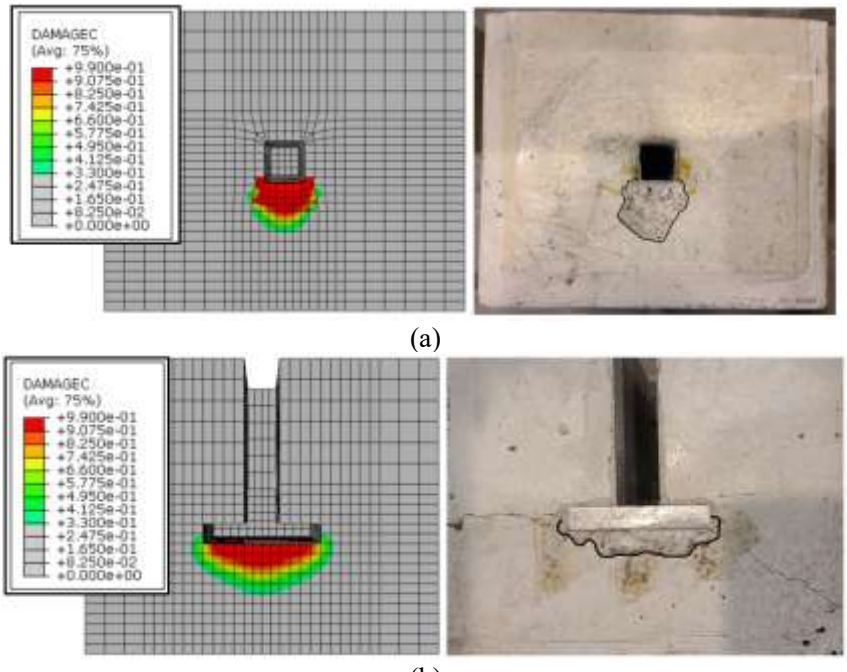

Fig. 22. Localised concrete crushing failure in reaction block (a) N60E15, (b) N60E15-Update

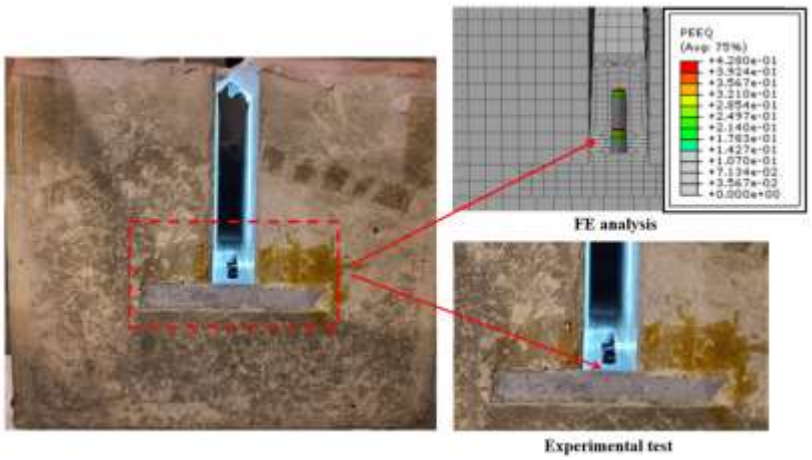

(a)

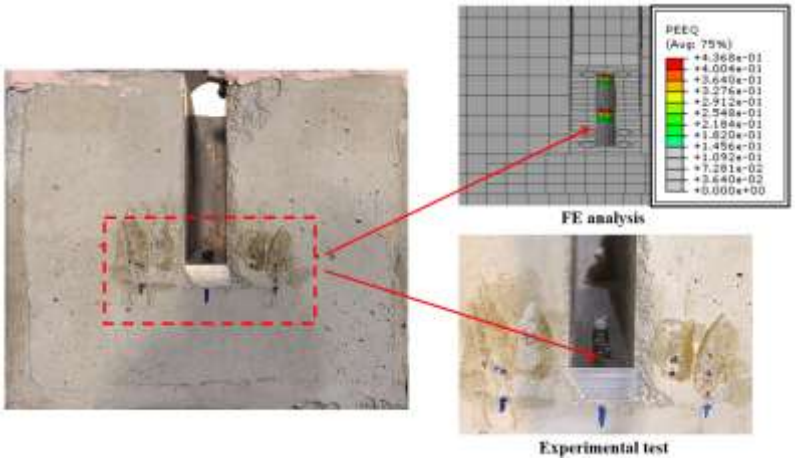

(b)

Fig. 23. Bolt fracture failure in loaded block (a) N60E15, (b) N60E15-Update.

Apart from failure modes, the deflection response of test specimens was also accurately predicted. Fig. 24 compares the load-deflection curves obtained from experimental tests and generated from FEA. Sudden load drops in load-deflection curves were due to sequential fractures of the first two bolts. Because of the dynamic response induced by bolt fracture, the predicted load-deflection curves slightly deviated from those recorded in experimental tests. However, these differences had little effect on the peak load of specimens, which were precisely predicted with a mean value of 1.01 and a coefficient of variation (CoV) of 0.04 as summarised in Table 10.

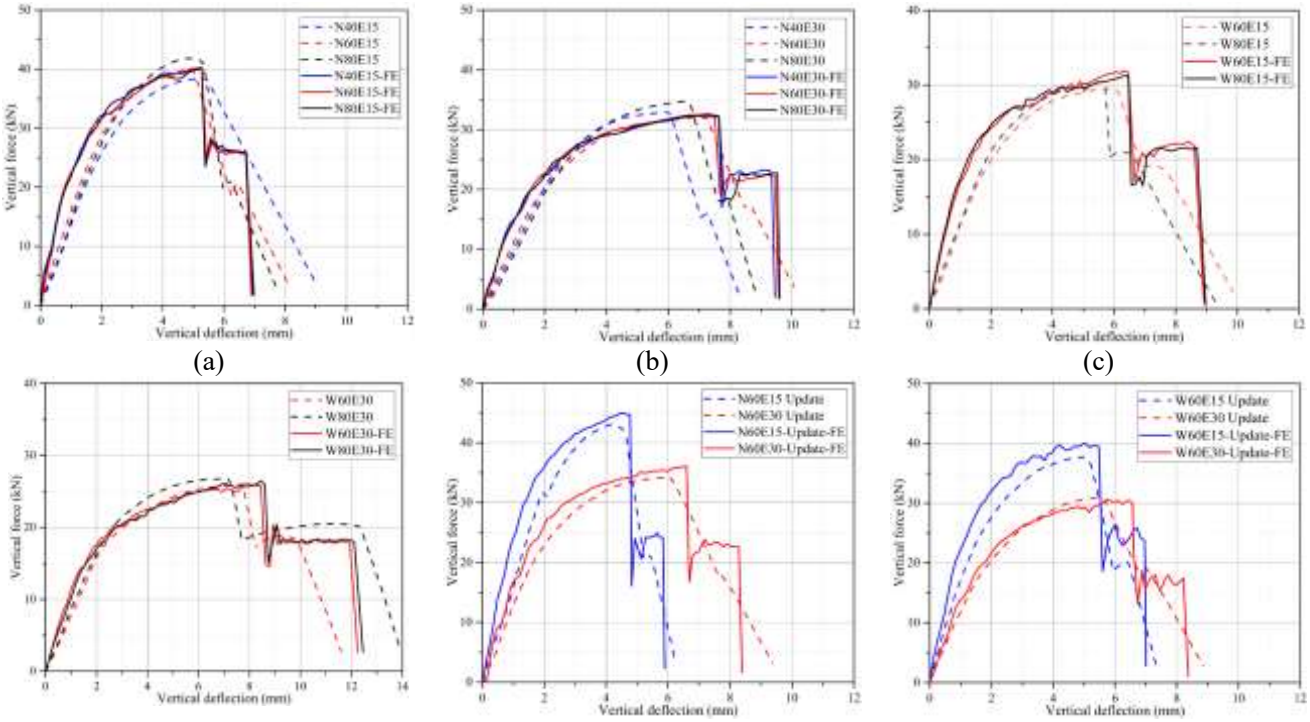

Fig. 24. Load-deflection curves from tests and FEA (a) N40(60, 80)-E15, (b) N40(60, 80)-E30, (c) W60(80)-E15, (d) W60(80)-E30, (e) N60E15(30)-Update, (f) W60E15(30)-Update.

Table 10 Ultimate loads from tests and finite element analysis.

Specimen ID	$N_{u,Test}$ (kN)	$N_{u,FE}$ (kN)	$N_{u,FE}/N_{u,Test}$
N40E15	38.45	40.35	1.05
N40E30	32.93	32.66	0.99
N60E15	40.02	40.34	1.01
N60E30	32.15	32.50	1.01
N80E15	41.86	40.08	0.96
N80E30	34.78	32.32	0.93
W60E15	29.51	31.97	1.08
W60E30	26.02	26.08	1.00
W80E15	30.37	31.22	1.03
W80E30	26.76	26.47	0.99
N60E15-Update	43.16	45.01	1.04
N60E30-Update	34.25	35.96	1.05
W60E15-Update	37.73	40.01	1.06
W60E30-Update	30.85	30.62	0.99
		Mean	1.01
		CoV	0.04

6.5. Parametric analysis

To further analyse the structural performance of concrete blocks with the updated narrow-section connection system, 27 models were developed and parameters including the stainless steel plate width, thickness and end distance were studied. The minimum thickness of the stainless steel plate was equal to the diameter of high-strength bolts to prevent thread stripping failure [43].

6.5.1. Stainless steel plate width

The width of the stainless steel plate influenced the contact area between concrete and steel and then further affected the failure mode. For models with the stainless steel plate of 10 mm thickness and 10 mm end distance, generated load-deflection curves and observed failure modes are shown in Fig. 25(a). For the model N40E10-T10-Update, severe crushing was caused in the loaded block due to high compressive stress of concrete at the joint surface. However, after increasing the width of the stainless steel plate, the ultimate load of models N60(80)E10-T10-Update was governed by bolt fracture instead of concrete crushing. In addition, horizontal tensile cracks were observed in the model N80E10-T6-Update as shown in Fig. 25(b). This was attributed to poor tensile resistance of concrete and the short edge distance between the embedded plate and the side of concrete block. As a result, applying a stainless steel plate with a width of 60 mm was recommended in developed finite element models.

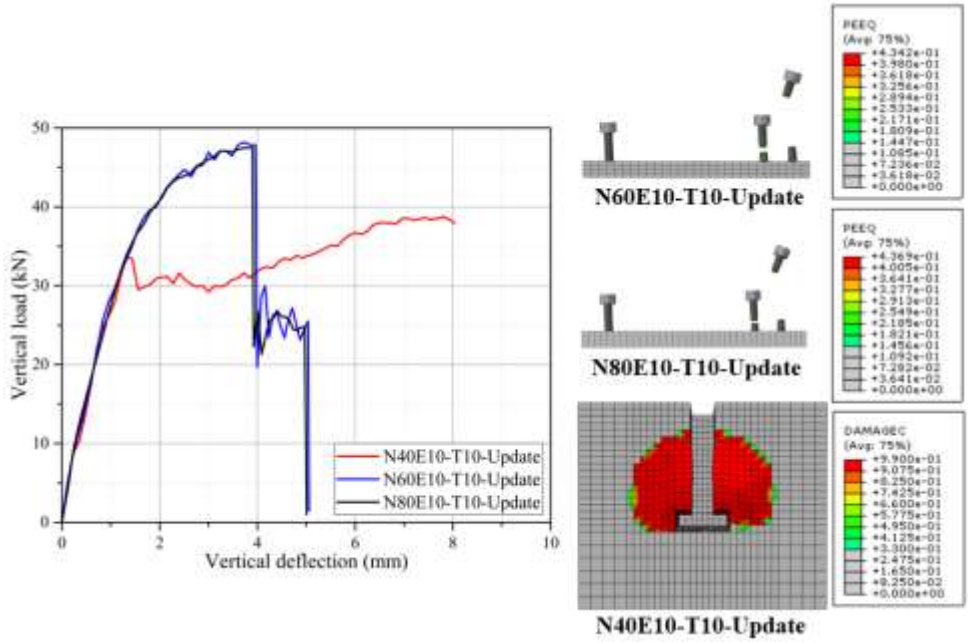

(a)

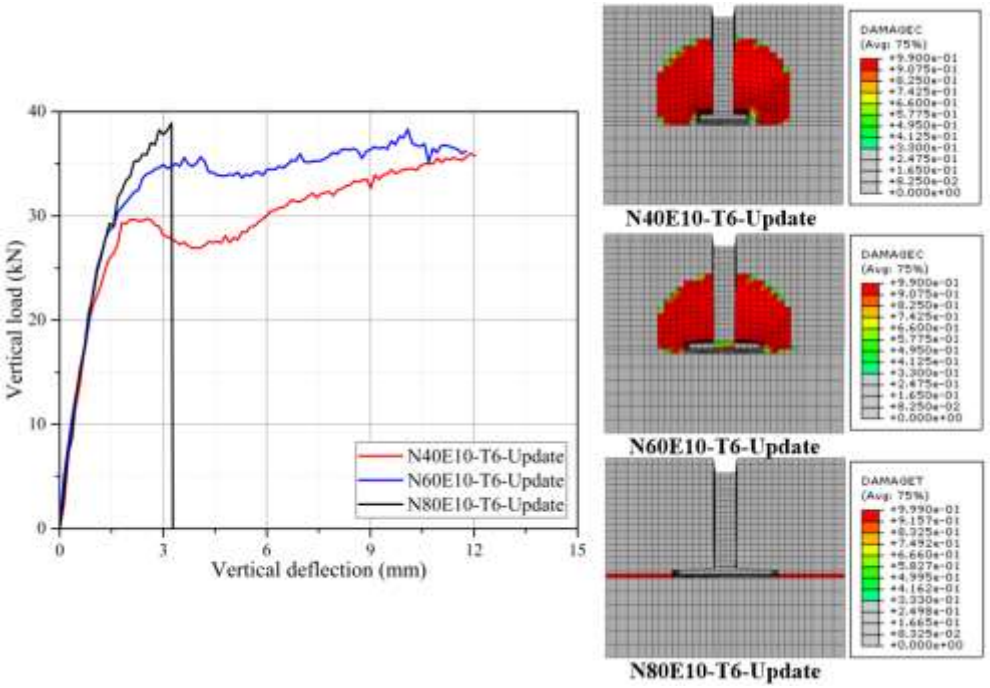

(b)

Fig. 25. Load-deflection curves of models with stainless steel plate of different widths (a) N40(60, 80)E10-T10-Update, (b) N40(60, 80)E10-T6-Update.

6.5.2. Stainless steel plate thickness

Under vertical load, the flexural deformation of the embedded stainless steel plate was primarily influenced by its thickness. For models with a stainless steel plate of 6 mm thickness, the large plate deformation induced severe concrete compressive stress concentration at the joint surface and thus caused localised concrete crushing and horizontal tensile cracks. However, after increasing the plate thickness to 10 mm, the flexural deformation of the plate was reduced and bolt fracture became the dominant failure as plotted in Fig. 26(a) and 26(b). Apart from failure modes, the thickness of the stainless steel plate also influenced the deflection response of developed models. Fig. 27(a) compares the vertical deflections of 6 mm and 10 mm thick stainless steel plates at 30 kN. Because of higher flexural stiffness, the flexural deformation of the 10 mm thick plate was significantly reduced, thereby resulting in enhanced initial stiffness as verified in Fig. 27(b). According to the parametric analysis results, the thickness of the stainless steel plate should be at least 10 mm to ensure high initial stiffness and prevent the occurrence of localised concrete crushing in the loaded concrete block.

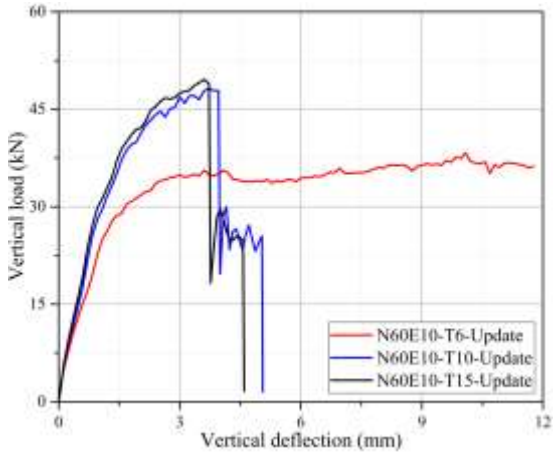

(a)

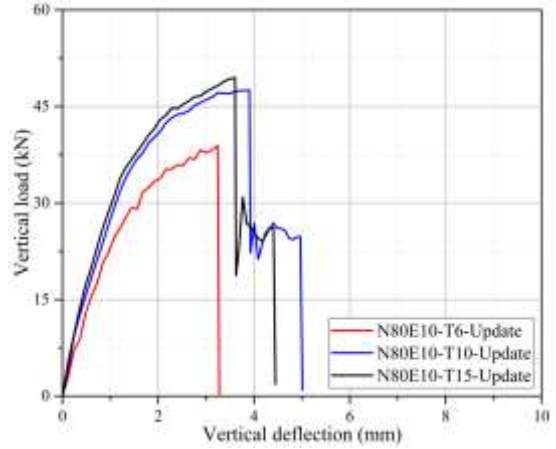

(b)

Fig. 26. Load-deflection curves of models with stainless steel plate of different thicknesses (a) N60E10-T6(10, 15)-Update, (b) N80E10-T6(10, 15)-Update.

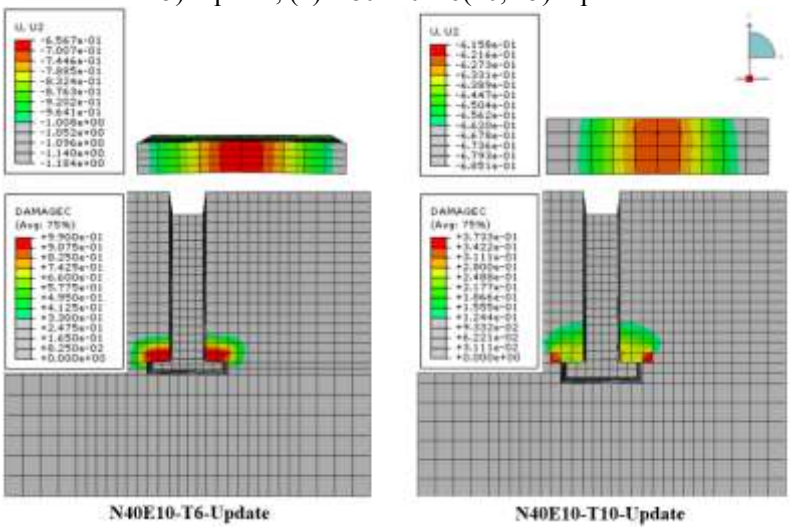

(a)

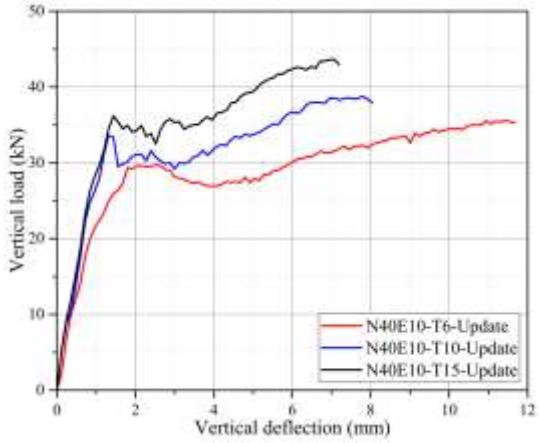

(b)

Fig. 27. Stainless steel plate deformation and load-deflection curves of models with stainless steel plate of different thicknesses (a) stainless steel plate deflection, (b) load-deflection curves.

6.5.3. Stainless steel plate end distance

Fig. 28(a) compares the load-deflection curves of models with the stainless steel plate of 60 mm width and 10 mm thickness. For the plate with an end distance of 10 mm, the flexural deformation of the stainless steel bar connection was minimised and large axial loads were developed in the first two bolts B1 and B2. As a result, the model N60E10-T10-Update exhibited the greatest initial stiffness and ultimate load. However, as displayed in Fig. 28(b), employing a stainless steel plate with a short end distance and a narrow width might increase the compressive stress of concrete and thus led to localised concrete crushing at the joint surface of the loaded block. Therefore, to improve the initial stiffness of the connection system and prevent concrete crushing failure in the loaded concrete block, the stainless steel plate with a width of 60 mm, a thickness of 10 mm and an end distance of 10 mm was suggested.

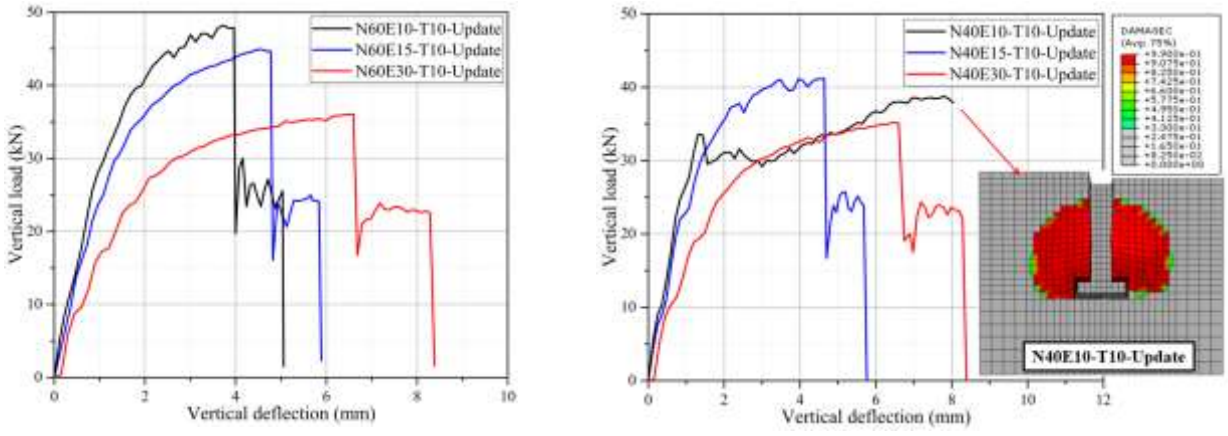

(a) (b)

Fig. 28. Load-deflection curves of models with stainless steel plate of varying end distances (a) N60E10(15, 30)-

6.6. Summary of design parameters

This section investigates the effect of the stainless steel plate dimension on the failure mode and deflection response of models equipped with the updated demountable stainless steel bar connection system. According to the parametric analysis results, the width, thickness and end distance of the stainless steel plate have significant influence on the failure mode of developed models. To prevent localised concrete crushing in the loaded block, the thickness and width of the stainless steel plate should be 10 mm and 60 mm, respectively. The end distance of the plate can be reduced to 10 mm to ensure a high initial stiffness of the connection system. In full-scale models, the suggested stainless steel plate thickness and end distance should be 1.67 times the bolt diameter, and the plate width-to-thickness ratio is optimised to 6.

7. Design load prediction

The main objective of developing the stainless steel bar connection system is to promote the reuse of individual pavement units. As described in Fig. 29, to prevent necking of the bolt shank that may hinder the disassembly of connection, the design load F_d of specimens is specified at the transferred load when the axial force of the first bolt B1 reaches the ultimate load. From the test results and FEA data, as shown in Fig. 30, two plastic hinges are developed near the second bolt and at the joint surface of the reaction block under the design load. Fig. 31 depicts the failure mechanism of the stainless steel bar connection, where F_{b1} and F_{b2} refer to the bolt forces of the first and the second bolt, respectively; M_{pl} denotes the plastic moment resistance of the stainless steel bar connection. To determine the design load of the connection, the moment equilibrium about the second bolt is established as expressed by Eqs. (19) to (22), where e_1 is the spacing between the first and the second bolt; m is the distance between the first bolt and the joint surface of the reaction block.

$$F_{\mathrm{d}}(m+e_1)=F_{\mathrm{b1}}e_1+2M_{\mathrm{pl}} \tag{19}$$

$$F_{\mathrm{b1}}=\sigma_{\mathrm{ub}}A_0 \tag{20}$$

$$F_{\mathrm{d}}=\frac{\sigma_{\mathrm{ub}}A_0e_1+2M_{\mathrm{pl}}}{m+e_1} \tag{21}$$

$$M_{\mathrm{pl}}=\frac{1}{4}w_{\mathrm{s}}h_{\mathrm{s}}{}^2\sigma_{0.2} \tag{22}$$

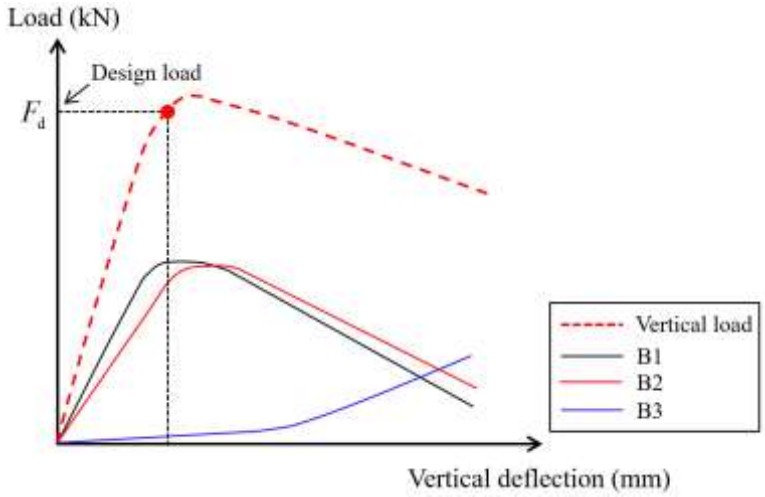

Fig. 29. Definition of the design load.

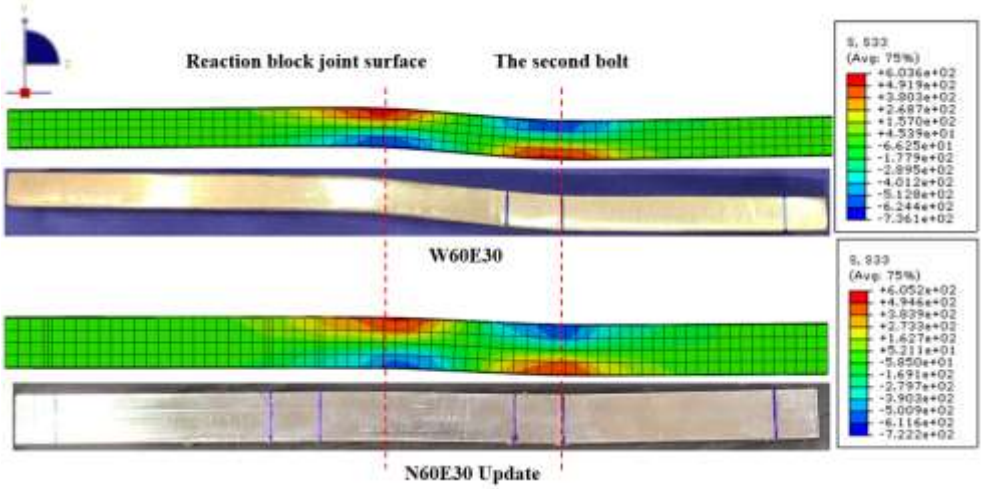

Fig. 30. Stress state of the stainless steel bar connection.

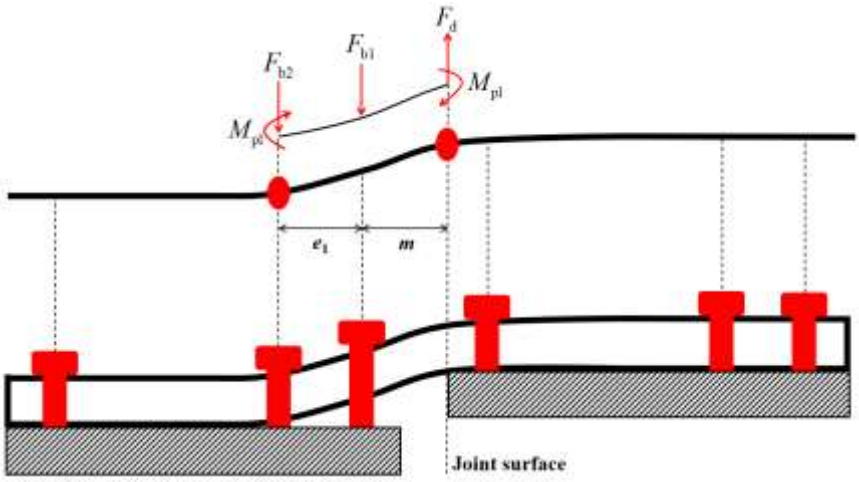

Fig. 31. Failure mechanism of the stainless steel bar connection.

In FEA, after obtaining the developed bolt loads, the design load F_d was acquired by subtracting the support force from the applied vertical load. Table 11 compares the design loads obtained from FEA and computed by the analytical prediction. A close agreement is achieved with a mean value of 0.99 and a coefficient of variation (CoV) of 0.05.

Table 11 Design loads obtained from FEA and analytical prediction.

Model ID	M_{pl} (kN·m)	$F_{d,Pred}$ (kN)	$F_{d,FE}$ (kN)	$F_{d,Pred}/F_{d,FE}$
N40E15	0.511	37.43	34.58	1.08
N60E15	0.511	37.43	34.95	1.07
N80E15	0.511	37.43	35.01	1.07
N40E30	0.511	27.40	26.68	1.03
N60E30	0.511	27.40	26.84	1.02
N80E30	0.511	27.40	26.85	1.02
N60E10-T10-Update	0.511	42.63	41.48	1.03
N80E10-T10-Update	0.511	42.63	41.20	1.03
N60E10-T15-Update	0.511	42.63	42.33	1.01
N80E10-T15-Update	0.511	42.63	42.20	1.01
N40E15-T10-Update	0.511	37.43	37.58	1.00
N60E15- T10-Update	0.511	37.43	37.50	1.00
N80E15- T10-Update	0.511	37.43	37.40	1.00
N40E15-T15-Update	0.511	37.43	37.79	0.99
N60E15-T15-Update	0.511	37.43	37.94	0.99
N80E15-T15-Update	0.511	37.43	38.05	0.98
N40E30- T10-Update	0.511	27.40	29.29	0.94
N60E30- T10-Update	0.511	27.40	29.70	0.92
N80E30- T10-Update	0.511	27.40	29.93	0.92
N40E30-T6-Update	0.511	27.40	28.17	0.97
N60E30-T6-Update	0.511	27.40	29.38	0.93
N80E30-T6-Update	0.511	27.40	29.38	0.93
N40E30-T15-Update	0.511	27.40	30.14	0.91
N60E30-T15-Update	0.511	27.40	30.25	0.91
N80E30-T15-Update	0.511	27.40	30.13	0.91
N60E10-T10-Update	0.511	42.63	41.48	1.03
N80E10-T10-Update	0.511	42.63	41.20	1.03
N60E10-T15-Update	0.511	42.63	42.33	1.01

N80E10-T15-Update	0.511	42.63	42.20	1.01
W60E15	0.366	30.39	28.13	1.08
W80E15	0.366	30.39	28.32	1.07
W60E30	0.366	22.25	21.95	1.01
W80E30	0.366	22.25	22.02	1.01
W60E15-Update	0.366	30.39	31.69	0.96
W60E30-Update	0.366	22.25	24.88	0.89
			Average	0.99
			CoV	0.05

8. Design recommendations

By carrying out experimental tests, FEA and the analytical prediction on the proposed demountable stainless steel bar connection system, the following design recommendations can be drawn:

1. High-strength bolts with a diameter of 10 mm should be applied in the full-scale specimen after considering the scale factor adopted in experimental tests.
2. The updated demountable stainless steel bar connection system is recommended because the embedded stainless steel plate can expand the contact area between concrete and steel and delay the occurrence of localised concrete crushing.
3. In the full-scale model, the section area and the length of the stainless steel bar connection should match those of a 32 mm diameter dowel bar. The width of the stainless steel bar connection should be 30 mm after considering the minimum edge distance in Eurocode 1993-1-8 [39]. The height of the connection is then adjusted to 27 mm to ensure a similar cross-section area and shear stiffness.
4. Based on the parametric analysis results, the thickness of the stainless steel plate should be 1.67 times the bolt diameter. Considering the width-to-thickness ratio of 6, 100 mm wide plates are suggested in full-scale specimens. The length of the plate is the same as the embedded length of a dowel bar equal to 230 mm. The recommended plate end distance is 1.67 times the bolt diameter to increase the initial stiffness of the demountable connection system.
5. The maximum shear force transferred by an individual pavement connection is 20 kN as recommended

466 in [20, 37]. It can be inferred from the test results that applying stainless steel plates of 100 mm width
467 can prevent the initiation of concrete crushing in practice. Furthermore, the design load of the
468 connection without the occurrence of bolt necking can be determined following the analytical approach
469 proposed in section 7.

470 **9. Conclusion**

471 In this paper, a demountable stainless steel bar connection system is proposed to promote the reusbility of
472 individual pavement units. For analysing the structural behaviour of the proposed connection system, both
473 experimental tests, FEA and the analytical model were conducted and developed. The following
474 conclusions are drawn based on the acquired data:

475 1. Bolt fracure and localised concrete crushing are typical failure modes of the specimens with the proposed
476 deomuntable connection system.

477 2. The stainless steel plate width, thickness and end distance affect the failure mode of models equipped
478 with the proposed deomuntable connection system.

479 3. When using a demountable stainless steel bar connection with a constant section area, increasing the
480 connection width from 16 mm to 22 mm can mitigate concrete compressive stress concentration under the
481 stainless steel tube by 29 percent. However, the ultimate load of specimens is impaired by more than 19
482 percent.

483 4. After replacing the stainless steel tube by a stainless steel plate in the updated connection system,
484 concrete compressive stress concentration in the loaded concrete block is mitigated by up to 71 percent.
485 Furthermore, the ultimate load of the updated specimens is also improved by more than 6 percent.

486 5. The ultimate load and initial stiffness of specimens with the updated connection system are enhanced by

increasing the stainless steel plate thickness and reducing the plate end distance.

6. To prevent localised concrete crushing in the loaded concrete block and maximise the initial stiffness of the proposed connection system, the thickness and the end distance of the stainless steel plate should be 1.67 times the bolt diamter. The recommended plate width-to-thickness ratio is 6 to ensure a sufficient contact area between concrete and steel.

7. To promote the reuse of precast concrete pavement units, the necking of bolt shank should be prevented. Therefore, the design load of the connection without the occurance of bolt necking is analytically predicted and validated.

Acknowledgements

The research work presented in this paper was supported by a grant from the Research Grants Council of the Hong Kong Special Administrative Region, China (Project no. R5007-18). The authors would like to sincerely thank the technical staff of the Structural Engineering Research Laboratory and Concrete Technology laboratory for their support.